ADANA
STU

REPUBLIC OF TURKEY
ADANA SCIENCE AND TECHNOLOGY UNIVERSITY
GRADUATE SCHOOL OF NATURAL AND APPLIED SCIENCES
DEPARTMENT OF NANOTECHNOLOGY AND ENGINEERING SCIENCES

STRUCTURAL AND OPTICAL PROPERTIES OF BULK AND QUANTUM WELL $GaAs_{1-x}Bi_x$ SEMICONDUCTORS

ELİF KUŞVURAN

MSc THESIS

Adana 2017

STRUCTURAL AND OPTICAL PROPERTIES OF BULK AND QUANTUM WELL $GaAs_{1-x}Bi_x$ SEMICONDUCTORS

KUŞVURAN Elif

Master of Science, Nanotechnology&Engineering Sciences

February 2017, 60 pages

ABSTRACT

The basis of wireless communications such as today's optoelectronic devices and mobile phone systems is the group III-V compound semiconducting materials. These materials can be used for optical fibers due to their band gap energies in the low dispersion and low optical loss window. The optical fibers have minimal loss in the wavelengths of 850 nm, 1310 nm and 1550 nm. For this reason, for long haul communications, 1550 nm window is used due to maximum transmission length of ~100 km while 1310 nm is preferred for short distance data communications (Mokkapati and Jagadish, 2009). In this thesis, structural and optical properties of Bi-containing crystal materials grown on GaAs substrate on various orientations by Molecular Beam Epitaxy (MBE) have been investigated. The samples that were grown as epilayer has Bi_x ($0<x<0.23$) content while quantum well's 1%, 2%, 3%, respectively. Compound semiconductor is produced by introducing Bi atoms into the GaAs and their optical properties were determined by temperature dependent photoluminescence measurements. It is presented that the structures are emitted at wavelength of 875-1000 nm which is close to the operation wavelength for telecommunication window. Under the guide of the previous investigation on epilayer structure, Bi- containing single quantum well structures were grown by MBE on (100) and then (311) B planes on semi-insulating (SI) GaAs substrate at various growth temperature due to investigate growth oriented structural, optical and electrical properties. Structural and morphological properties were determined by X-ray diffractometer (XRD), Atomic Force Microscopy (AFM), Raman measurement. Optical phonon energies that induced by vibration of the structure according to introducing Bi content and high index plane growing were calculated using Raman measurement. As a result, it was experimentally reported that such materials have potential to be used as laser design for fiber optic communications for the first time in the current thesis.

Key words: *Quantum well, AFM, XRD, PL, Raman spectroscopy*

BULK VE KUANTUM KUYU GaAs$_{1-x}$Bi$_x$ YARIİLETKEN ALAŞIMLARININ YAPISAL VE OPTİK ÖZELLİKLERİNİN İNCELENMESİ

KUŞVURAN Elif

Yüksek Lisans, Nanoteknoloji ve Mühendislik Bilimleri

Şubat 2017, 60 sayfa

ÖZET

Günümüz optoelektronik aygıtların ve cep telefonu sistemleri gibi kablosuz haberleşmenin temelini III-V grubu bileşik yarıiletken malzemeler oluşturmaktadır. Bu malzemelerin bant enerji değerleri, optik fiberler için uygun olan düşük dağılımlı ve düşük düşük kayıp seviyesindedir. Optik fiberler, 850 nm, 1310 nm and 1550 nm dalga boylarında minimum kayba sahiptirler. Bu sebeple, uzun mesafeli iletişimlerde, ~ 100 km'lik maksimum iletim uzunluğuna sahip olması nedeniyle 1550 nm kullanılırken, kısa mesafeli veri iletişimi için 1310 nm tercih edilir. Proje kapsamında, Moleküler Beam Epitaxy ile GaAs alttaş üzerine farklı yönelimlerde büyütülmüş, Bi içeren kristal malzemelerin yapısal ve optik özellikleri incelenmiştir. Proje kapsamında, yürütülen deneylerde, araştırılan malzeme sistemleri epilayer numunelerde, Bi$_x$ ($0<x<0.23$) miktarlarında, kuantum kuyulu Bi içeren yapılarda ise %1, %2, %3 Bi konsantrasyonlarındadır. Yapılan çalışmalar sonucunda, bileşik yarıiletkenler GaAs yarıiletkenine Bizmut atomu ilavesi ile oluşturulmuş ve optik özellikler sıcaklığa bağlı foto ışıma deneyleri ile ortaya konmuştur. Yapıların telekomünikasyonun çalışma penceresine yakın olan 875-1000 nm dalga boyunda emisyona sahip olduğu ortaya konmuştur. Proje öncesi, epilayer olarak büyütülen yapılardan elde edilen bulgular ışığında, Bi içeren yapılar MBE tekniği kullanılarak, yarı yalıtkan GaAs alttaş üzerine farklı büyütme sıcaklıklarında önce (100) düzlemi üzerine tek kuantum kuyusu olarak büyütülmüştür. Daha sonra, aynı yapısal özelliklere sahip numuneler, (311) B doğrultusunda büyütülerek, yapısal, optik ve elektriksel olarak büyütme oryantasyonuna bağlı özellikler araştırılmıştır. Yapısal ve morfolojik özellikler, X-ışını difraktometresi, Atomik Kuvvet Mikroskobu, Raman ölçümleri yapılarak gerçekleştirilmiştir. Kuantum yapıların kristal kalitesi, örgü parametresi, büyütme düzlemleri XRD tekniği ile yüzey morfolojisi ise AFM tekniği kullanarak belirlenmiştir. Yapısal titreşim sonucu oluşan optik fononların enerjileri, ilave edilen Bi atom miktarına ve high index plane (311)B'de büyütmeye bağlı olarak ayrı ayrı Raman tekniği ile belirlenmiştir. Ayrıca, birçok tekrarlar yaparak elde edilen yüksek kalitedeki GaAsBi/GaAs tek kuantum kuyu yapıların kızılötesi bölgesinde ışınım yapan lazer tasarımında kullanılabilme potansiyeli olabileceği ilk kez bu tezde rapor edilmiştir.

Anahtar Kelimeler: *Kuantum kuyusu, AFM, XRD, PL, Raman spektroskopisi*

ACKNOWLEDGEMENTS

I would like to declare my biggest gratitude to my supervisor, Assoc. Prof. Dr. Mustafa Güneş, to accept me for this challenging thesis and give me chance to work on this excellent research field. His kind discussion and suggestions made my thesis work possible to be well-wrapped.

I would like to thank TUBITAK for providing financial support with the project number 114F294.

I am greatly indebted to Prof. Dr. Mohamed Henini from University of Nottigham, School of Physics & Astronomy Department to grow the investigated structures.

I would like to thank to Assoc. Prof. Dr. Uğur Serincan and Ph.D. student Burcu Arpapay for their warm welcome to Nanoboyut Research Laboratory in Anadolu University.

My deepest gratitude goes to my parents and all of my family members for their love, well wish and encouragement that helped me all time to move forward, even staying far from them in abroad. I would like to express my special thanks to my mother who accompanied me whenever I needed. My father always supported me during all steps I took and my brother for encourage me to be a research assistant in Adana STU. I am also very grateful to my better half Çağlayan Kuşvuran for his sincere support.

This thesis was financially supported by TUBİTAK with project number of 114F294.

TABLE OF CONTENTS

ABSTRACT .... **i**

ÖZET .... **ii**

ACKNOWLEDGEMENTS .... **iii**

TABLE OF CONTENTS .... **v**

LIST OF FIGURES .... **viii**

LIST OF TABLES .... **x**

NOMENCLATURE .... **xi**

CHAPTER 1

1. INTRODUCTION 1

1.1 History of III-V Semiconductors 1

CHAPTER 2

2. BACKGROUND 6

2.1 Introduction 6

2.2 Elemental and Compound Semiconductors 7

2.3 Crystal Structure of GaAs and $GaAs_{1-x}Bi_x$ Alloys 10

2.4 Material Parameters of III-Vs 11

2.5 Band Structure of Semiconductors 12

    2.5.1 Direct and indirect band gap semiconductors 12

2.6 Optical Properties of GaAs and $GaAs_{1-x}Bi_x$ Alloys 15

2.7 Substrates 18

2.8 Low Dimensional Structures 18

    2.8.1 Two dimensional systems 20

CHAPTER 3

3. EXPERIMENTAL TECHNIQUES 21

3.1 Introduction 21

3.2 Material Growth Techniques 21

3.2.1 Bulk crystal growth 21
3.2.2 Epitaxial crystal growth 22
3.2.2.1 Liquid phase epitaxy (LPE) 22
3.2.2.2 Vapor phase epitaxy (VPE) 23
3.2.2.3 Metal organic chemical vapor deposition (MOCVD) 24
3.2.3 Molecular beam epitaxy (MBE) 25
3.2.3.1 General principles of solid source-MBE 25
3.3 Material Growth 28
3.4 Structural Characterization 29
3.4.1 Atomic force microscopy (AFM) 29
3.4.1.1 Experimental set-up for AFM 29
3.4.2 High resolution X-ray diffraction (HRXRD) 30
3.4.2.1 Experimental set-up for XRD 31
3.5 Optical Characterization 32
3.5.1 Photoluminescence spectroscopy 32
3.5.1.1 Photoluminescence experimental set-up 34
3.5.2 Raman spectroscopy 35
3.5.2.1 The basis of the raman effect 35
3.5.2.2 Experimental set-up for raman 37

CHAPTER 4

4. RESULTS AND DISCUSSION 38
4.1 Introduction 38
4.2 X-ray Diffraction (XRD) Results 40
4.2.1 High Resolution X-ray Diffraction (HRXRD) Results 41
4.3 Atomic Force Microscopy (AFM) Results 45
4.4 Photoluminescence (PL) Results 46
4.5 Raman Spectroscopy Results 50

CHAPTER 5

5. CONCLUSIONS 54

REFERENCES.. 56

LIST OF FIGURES

Figure 1.1 Schematic of band gap change by Bi concentration 2
Figure 1.2 Valance band dispersion curve of GaAsBi 4
Figure 2.1 A section of the Periodic Table showing the elements involved in the formation of semiconductors.. 7
Figure 2.2 Crystal structure of silicon and germanium 8
Figure 2.3 Band gap versus lattice constant for semiconductors 8
Figure 2.4 Zinc blende (ZnS) lattice structure 9
Figure 2.5 Wurtzite lattice structure 9
Figure 2.6 Face centered cubic unit cell of GaAs... 10
Figure 2.7 Crystal conversion of Zinc Blende $GaAs_{1-x}Bi_x$ 10
Figure 2.8 Schematic illustration of direct and indirect band gap semiconductor 12
Figure 2.9 Schematic illustration of Brillouin Zones 14
Figure 2.10 Conduction-band electron effective mass m* versus band gap energy (E_g) for various compound semiconductors... 15
Figure 2.11 Optical loss versus wavelength.. 16
Figure 2.12 Band gap versus lattice constant for various III-V ternary semiconductors, Including GaAs/GaAsBi. 16
Figure 2.13 Schematics of the density of states as a function of dimensionality 19
Figure 2.14 Illustration of a two dimensional system localization in the real space 20
Figure 3.1 Schematic of bulk crystal growth (CZ technique) system 22
Figure 3.2 A schematic illustration of the LPE growth for general materials.................... 23
Figure 3.3 VPE growth reactors.. 23
Figure 3.4 Schematic illustration of an MOCVD system.. 24
Figure 3.5 Solid Source MBE system 26
Figure 3.6 Solid source MBE growth chamber.. 26
Figure 3.7 RHEED Intensity Oscillations.. 27
Figure 3.8 A typical RHEED pattern 28
Figure 3.9 RHEED intensity oscillations of during GaAs and AlAs growth 28
Figure 3.10 Layer structure of the investigated structures grown by MBE........................ 29
Figure 3.11 Schematic diagram of a Tapping Mode AFM with basic components 30
Figure 3.12 Proof demonstration of Bragg’s law 31
Figure 3.13 Schematic of the experimental setup showing the optical path of the X-ray beam 32
Figure 3.14 Possible radiative recombinations in semiconductors 33
Figure 3.15 Mechanisms involved during PL emission 34

Figure 3.16 Experimental set-up for Photoluminescence 35
Figure 3.17 Energy level schema demonstrating the states included in Raman scattering 36
Figure 3.18 Experimental set-up for Raman Spectroscopy 37
Figure 4.1 Bulk GaAs and GaAsBi structures 39
Figure 4.2 Layer structure of $GaAs_{1-x}Bi_x$/GaAs single-quantum well semiconductors 39
Figure 4.3 XRD spectra of **(a)** Bulk $GaAs_{1-x}Bi_x$, **(b)** (100) and **(c)** (311) B Quantum well $GaAs_{1-x}Bi_x$ /GaAs structures 41
Figure 4.4 Symmetric rocking curves of $GaAs_{1-x}Bi_x$ SQWs 42
Figure 4.5 AFM images of **(a)** Ms823 and **(b)** Ms824 bulk $GaAs_{1-x}Bi_x$/GaAs structures 45
Figure 4.6 AFM images of $GaAs_{1-x}Bi_x$/GaAs SQW **(a)** 4144c (1%Bi), **(b)** 4145c (2%Bi) and (c) 4153c (3%Bi) 46
Figure 4.7 AFM images of $GaAs_{1-x}Bi_x$/GaAs SQW (a) 4151 (1%Bi), (b) 4152 (2%Bi) and (c) 4154 (3%Bi) 46
Figure 4.8 PL spectra of GaAsBi QW structures at temperatures between 8 K and 300 K growth on (a) (100) and (b) (311) direction 47
Figure 4.9 PL spectra of GaAsBi QW structures at power values of 0.083mW-51mW growth on (a) (100) and (b) (311) direction 48
Figure 4.10 Photoluminescence spectra of quantum well samples at 8 K 49
Figure 4.11 Raman spectra of $GaAs_{1-x}Bi_x$ grown on (100) (x= 1%, 2% and 3%) 50
Figure 4.12 Raman spectra of $GaAs_{1-x}Bi_x$ grown on (311) B (x= 1%, 2% and 3%) 51
Figure 4.13 Normalized Raman spectra of GaAs1-xBix grown on (311) B (x = 1%, 2% and 3%) 52

LIST OF TABLES

Table 2.1 Properties of Gallium, Arsenic and Bismuth 11
Table 2.2 Lattice parameter and band gap of common III-V semiconductor materials 17
Table 4.1 List of samples investigated in this work with bismuth concentration 40
Table 4.2 The measured and calculated X-ray diffraction parameters for $GaAs_{1-x}Bi_x$ 44
Table 4.3 The thickness of GaAs cap layers calculated from X-ray rocking curve measurements for $GaAs_{1-x}Bi_x$ SQWs 44
Table 4.4 Photoluminescence peak energies at 8 K 49
Table 4.5 Optical phonon energies of Bi-containing structures 53

NOMENCLATURE

Si	Silicon
Ge	Germanium
Ga	Gallium
As	Arsenic
Zn	Zinc
S	Sulfur
Al	Aluminum
In	Indium
P	Phosphor
Sb	Antimony
N	Nitrogen
Bi	Bismuth
UV	Ultraviolet
IR	Infrared
GaAs	Gallium Arsenide
GaBi	Gallium Bismide
GaN	Gallium Nitride
AlAs	Alluminium Arsenide
ZnS	Zinc Sulphide
InP	Indium Phosphide
GaP	Gallium Phosphide
GaAsBi	Gallium Arsenide Bismide
GaAlAs	Gallium Alluminium Arsenide
InGaAs	Indium Gallium Arsenide
GaInAs	Gallium Indium Arsenide
GaInNAs	Gallium Indium Nitride Arsenide
GaInAsP	Gallium Indium Arsenide Phosphide
LED	Light Emitting Diode
Laser	Light amplification by stimulated emission of radiation
PL	Photoluminescence
FWHM	Full Width at Half Maximum
DMS	Diluted Bismuth Semiconductors
meV	Milli-electron Volts
BAC	Band-Anti Crossing
VBAC	Valance Band-Anti-Crossing

EN	Energy Level
CB	Conduction Band
VB	Valance Band
AFM	Atomic Force Microcopy
XRD	X-ray Diffraction
µm	Micrometer
DELTA	Spin-orbit Splitting Energy
E_{Bi}	Localized Energy Level of Bismuth
E_p	Kane Energy
E_g	Energy Bandgap
QW	Quantum Well
PR	Photoreflectance
DFT	Density Functional Theory
eV	Electron Volt
HH	Heavy Hole
LH	Light Hole
E	Energy of Photon
p	Momentum
h	Planck Constant
$\hbar$	Planck constant divided by 2π
c	Speed of Light
λ	Wavelength of Photon
k	Frequency of Photon
E_c	Conduction Band Edge
m*	Effective Mass
$\dot{A}$	Lattice Parameter
MBE	Molecular Beam Epitaxy
RF-MBE	Plasma Assisted Molecular Beam Epitaxy
MOVPE	Metal-Organic Vapour Epitaxy
QD	Quantum Dot
2D	Two Dimensional
LPE	Liquid Phase Epitaxy
VPE	Vapor Phase Epitaxy
CZ	Czochralski
(CH3)3Ga	Triethyl Gallium
AsH3	Arsine

UHV	Ultra High Vacuum
RHEED	Reflection High-Energy Electron Diffraction
keV	Kiloelectron Volt
STM	Scanning Tunneling Microscopy
nm	Nanometer
RMS	Root Mean Squared
HRXRD	High Resolution X-ray Diffraction
SQW	Single Quantum Well
Pex	Excitation Power
mW	Milliwatt
TO(Γ)	Transverse Optical Mode
LO(Γ)	Longitudinal Optical Mode
DATO	Disorder-Activated TO

CHAPTER 1

1. INTRODUCTION

1.1 History of III-V Semiconductors

III-V semiconductors are preferred for the comprehension of today's optoelectronic devices, especially in defense industry and nanotechnology applications such as IR detector, LED, Laser etc. and this class of materials is also dominant in components for wireless communication. In communication systems, minimal loss of information transfer through the fiber optic cable is strongly depended on the laser wavelength that must be in the range between 1200 nm and 1600 nm (Azadeh, 2009). There are laser systems which consist of the semiconductor materials that emit at this wavelength ranges. The lasers which are formed by using GaInAsP/InP materials are more favorable due to their easy production and desire power output features. Moreover, the band gap of these systems which determines the emission wavelength is adjusted by using those materials to use as a laser to transfer the information. They have been also used as photodiodes and development of optical amplifiers (Hsieh and Shan, 1977; Oe et al., 1977; Thijs et al., 1994). However, due to high temperature sensitivity, less stable power output and high cost, the production of those materials has been limited to design optoelectronic devices.

In 1996 Kondow et al. proposed novel materials named as GaInAs and GaInNAs. By introducing N into the host GaInAs semiconductor induced to shrinkage the band gap energy as well as improvement in the carrier mobility which is crucial to develop any electronic devices. Since then, such materials system has become the focus of the researches. Introducing diluted nitrogen (N) into the group of III-Vs provides superior properties to the structure but it causes the formation of defects in the structure (Erol et al., 2003). These defects are induced the reduction both optical and electrical performance and the effect of nitrogen introduction is increased with increasing nitrogen concentration. This decrease in optical quality was experimentally demonstrated. The amount of Nitrogen introduced in the material induce an expansion FWHM of PL signal reducing the signal quality. (Erol et al., 2003; Schneider et al., 2000). The superiority provided by the band structure and enabling the GaAs-based device development in this material system. However, due to the disadvantage of the electronic transport caused by the presence of nitrogen has negative effects on device performance.

Structures that called diluted bismuth semiconductors (DMSs) obtained by introducing diluted bismuth (Bi <5 %) into GaAs or GaInAs semiconductors. Band structure of diluted bismuth semiconductor materials systems lattice structure is modified by the presence of Bi and it has different physical properties from band structure of other conventional semiconductors (GaAlAs, GaInAs etc.). Band gap energy decreases in the range of 70-90 meV/%Bi and spin-orbit energy increases with introducing bismuth into the lattice of host (Francoeur et al., 2003; Fluegel et al., 2006). Because of decrease in band gap energy and increase in spin-orbit energy, Bi containing semiconductors have high potential to use band gap changes that provides to use these materials long wavelength optoelectronic devices, improve GaAs based lasers which are emitted light at between 1.26-1.34 μm that are corresponding to the telecommunication working windows with lowest loses, use them as detectors of optical communication and optical amplifier. Due to low growth temperature and strain effect of Bi containing semiconductors it is so hard to grow high quality crystal. III-V (Bi) alloys are considered to be a good candidate for near infrared detectors as well as terahertz laser and detectors as a result of emitting the terahertz emission (Bertulis et al., 2006). It is a sign to use these materials systems in spintronic based device design because of spin-orbit splitting energy increases with addition of Bi. Increase in spin-orbit energy causes the rise in conduction band and valance bands offsets that hinder the escape of carriers which are exited with thermal energy. If the band structure and the magnitude of the band discontinuities of the such alloys systems was deeply understood, the confinement of the carriers in the quantum well and transport properties would be determined.

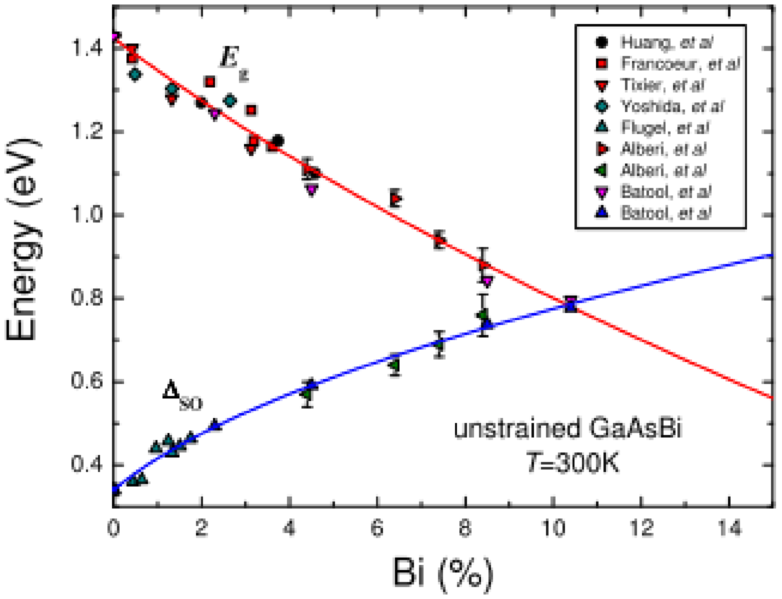

Figure 1.1 Schematic of band gap change by Bi concentration (Sweeney and Jin, 2013).

Although, electronic band structure changes by introducing dilute concentration of Bi atom in GaAs is still not understood, Band-Anti Crossing (BAC) Model which is developed for

N containing GaAs structures is modified for Bi containing III-V materials systems that is called as Valance Band-Anti-Crossing (VBAC) Model. According to this model, band structure of the semiconductor material system containing dilute amounts of nitrogen undergoes modification by the presence of nitrogen participating lattice. When Nitrogen (N) which participate the sub-lattice of the group V element of III-V group of semiconductor and replaced atom (In GaInNAs, N replaces As) is compared in size and electronegativity, N size is so smaller than As and its electronegativity is so bigger than As. Therefore, it creates a local perturbation in the lattice. N is an acceptor contribution in GaAs and GaInAs and its localized energy level (EN) is also located above the conduction band. However, localized energy level of nitrogen which introduced into the alloy structure is resonant with conduction band and as a result of the strong nitrogen perturbation, the host semiconductor conduction band is divided into two E- and E+. It has been proposed as a theoretically, Bismuth that participate the sub-lattice of group V element of III-V group of semiconductor is consisted a localized energy level (E_{Bi}) is located near the valance band like nitrogen perturbation effect on conduction band and gets resonant with host semiconductor (GaAs) valance band so valance band of host semiconductor is divided into two E- and E+. (Figure 1.2) (Alberi et al., 2007). However, recently published reports have revealed that introduction of the Bi into the structure modifies both conduction and valance, but theory is not fully understood yet (Usman et al., 2011; Kopaczek et al., 2015; Polak et al., 2015).

The matrix element is used to determine the E_{HH} and E_{LH} energies (Broderick et al., 2015).

$$H = \begin{bmatrix} E_{CB} & 0 & \sqrt{2}U & -U & 0 & 0 \\ & E_{HH} & 0 & 0 & V_{Bi} & 0 \\ & & E_{LH} & Q & 0 & V_{Bi} \\ & & & E_{SO} & 0 & 0 \\ & & & & E_{Bi}^{HH} & 0 \\ & & & & & E_{Bi}^{LH} \end{bmatrix} \tag{1}$$

where V_{Bi} is the matrix element of Bi composition related, E_{CB} is conduction band edge energy, E_{HH} and E_{LH} energies of HH and LH, respectively. E_{Bi}^{LH} and E_{Bi}^{HH} demonstrates the energies of the LH- and HH-like Bi-dependent impurity states.

Examining the equation (1) it gives the equations (Broderick et al., 2015)

$$E_{CB}(x,e) = \tilde{E}_{CB}(x,e) \tag{2}$$

$$E_{\pm}^{HH}(x,e) = \frac{\check{E}_{HH}(x,e)+E_{Bi}^{HH}}{2} \pm \sqrt{\left(\frac{\check{E}_{HH}(x,e)-E_{Bi}^{HH}}{2}\right)^2 + |V_{Bi}|^2} \tag{3}$$

where $\breve{E}_{HH}(x,e)$ and $\tilde{E}_{CB}(x,e)$are shifts which induced by the band edge energies.

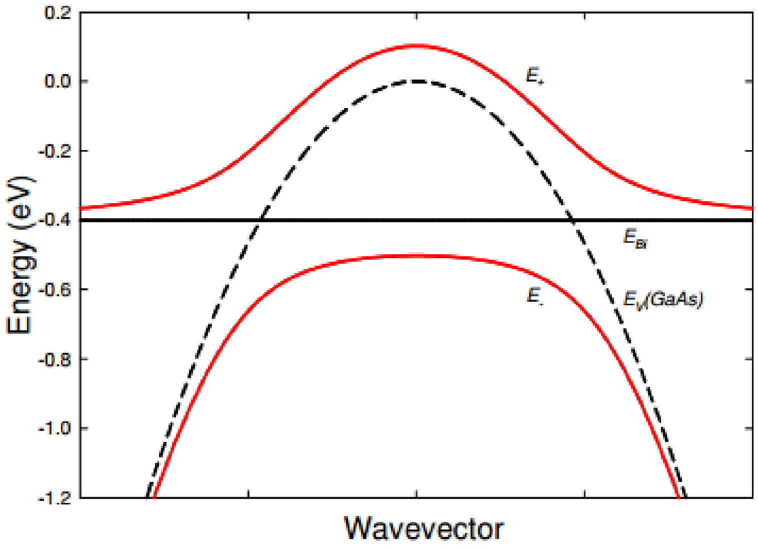

Figure 1.2 Valance band dispersion curve of GaAsBi (Alberi et al., 2007).

As a result of usage in optoelectronic technology, there has been intense research activities on those structures especially about determination optical properties and examination of band structure for more than three years (Kopaczek et al., 2015). The presence of bismuth is contributing to the narrowing of band gap as well doesn't cause the decrease in the carrier mobility, these materials are superior than N-containing materials (Pettinari et al., 2013). Semiconductor devices with high mobility are preferred in the device application. Thus, it is important that technological feasibility of producing superior optoelectronic devices with no reduction in mobility despite the presence of Bi. However, still no clearly understood of its band structure and low growth temperature, there are deficiencies associated with the use of technological applications of those structures. Depending on the difference between the largest atomic numbers (Bi Z= 83, Ga Z= 31 and As Z = 33) Bi shows low associativity property in GaAs. Consequently, Bi droplets occur on the crystal surface causing defects into the structure (Sales et al., 2011).

Defects is originated from Bi will be investigated within the scope of the thesis. For this purpose Bi-containing semiconductor material is grown on high-index planes so as to specify the effect of growth orientation on the material properties. The expectation is reduced the number of the non-radiative transition which may be originated Bi-related defects and increase improving the Bi incorporation with high quality crystal. The high-index (311) B oriented samples are investigated to compare conventionally grown (100) orientation in terms of optical, vibrational and electronic properties. A recent study shows that the incorporation of Bi atoms into III-V host modifies both the conduction band (CB) and the valence band (VB) (Polak et al., 2015). On the other hand, the defects which result from the incorporation of Bi into the structure are not exactly revealed in literature and there is a huge gap in this regard. Within the scope of thesis, determination of defects into the structure and the grown temperature effect in diluted bismuth semiconductors for reducing the defects impact will be on research. For GaAsBi/GaAs structures, it is impossible to use electronic devices production without attaining growth parameters, defects, impurities and perfect surface morphology. In this sense, there is very limited experimental study on optical properties of GaAsBi semiconductor system in the literature. In the studies, effects of different concentrations of Bi are investigated but different growth, annealing temperature and time were not available in a comprehensive research on the impact of high growth index. In addition, structural properties of $GaAs_{1-x}Bi_x/GaAs$ Quantum Well which is presented in Figure 3.10 having 10 nm well width with various Bi content (Bi% = 1%, 2%, 3%) grown on (100) and (311) B directions was grown for the first time. Structures which firstly grown on as a quantum well in terms of high index is not available in the literature.

The first phase of this thesis to determine the band gap of GaAsBi (at various Bi content) and Bi free GaAs structures that grown on different orientation, temperature and grown temperatures. Photoluminescence measurements were performed for optical characterization of samples. Band discontinuities and effective carrier masses will be determined. Moreover, structural properties of those structures were investigated by AFM, XRD. Orientation dependent structural properties such as surface roughness, grain size, d, 2Q so on. Those parameters play important role in optimizing the best crystal structures. Investigating carrier transport mechanism in terms of different concentrations, orientation and heat treatment factors, thesis proposal was filled an important gap in the literature on this subject. Thesis outcomes in prospective studies that will provide the best device performance contribute to the determination of modulation doped GaAsBi/GaAs quantum well structure. Also, it is important to fill the gap in terms of the design of the lasers make radiation in the infrared region.

CHAPTER 2

2. BACKGROUND

2.1 Introduction

The current chapter is aimed to determine structural, optical and electrical properties of GaAs and Bismuth-containing GaAs semiconductors. In the past decades, much study has been dedicated for realization of uncooled 1.3 μm laser diodes based on N-containing III-V semiconductors. The InGaAs/GaAs quantum well laser is restricted by the critical thickness and can only gain lasing at wavelengths up to 1.24 μm at room temperature. The incorporation of Bi into III–V QWs has the possibility to accomplish 1.3 μm light emission (Kopaczek et al., 2015). The incorporation of %Bi into III-V ternary compound semiconductors induce the band gap reduction from ~34 meV to ~88 meV while the band gap reduction for %In is only 11 meV as reported (Francoeur et al., 2003) and redshift the emission wavelength, all of which are important for optoelectronic devices. Such as diode lasers, photodetectors, long wavelength emitters, other optoelectronic and spintronic-based devices. Due to vigorous nuclei potential and great kinetic energy, electron velocity gains to the level of light speed providing $GaAs_{1-x}Bi_x$ spin-orbit splitting energy (Δ_{SO}) enhancement with introducing the Bi into GaAs (Tong et al.,2014). A low temperature sensitivity of band gap which preferred for infrared emitters and photodetectors is ensured by enhancement of spin-orbit splitting energy (Lu et al., 2008).

Spin-orbit splitting energy rely on strongly the exact determination of the $Land\acute{e}$ g-factor is a geometric factor that originates in the measurement of the magnetic interaction (Nave, 2016) so the photoluminescence polarization oscillations can be determined under external transverse magnetic field. Through the tilting the excitation beam and result of GaAs polarization dynamics, g-factor can be determined. Introducing the small amount of Bi in GaAs result in enhancement of g-factor. The GaAsBi g-factor nearly double of the GaAs g-factor (Mazzucato et al., 2013). The electron g-factor can be estimated by the following expression:

$$g = 2 - \frac{2}{3}\frac{E_p\Delta_{so}}{E_g(E_g+\Delta_{SO})} \;; \qquad (4)$$

E_p is the Kane energy, E_g is the energy bandgap, and Δ_{SO} the SO splitting energy.

Though, the incorporation of Bi into QWs is more complicated than that into bulk alloys. For instance, because of Bi melting point (271.5°C) is really lower than the GaAs melting point (1248°C), during the growth process although some defects such as Bi droplets may arise due to low growth temperatures, the low temperatures are required for high compositions (>1%Bi) (Lu et al., 2008). Bi incorporation in GaAs is anticipating with Bi-related defects lie in the valence band (VB) owing to some Bi properties such as bigger atom radius and lower electronegativity than As.

In this study, optical properties of $GaAs_{1-x}Bi_x$ QWs via different Bi concentrations and growth directions by using PL in temperature range of 8-300 K and various excitation power was determined.

2.2 Elemental and Compound Semiconductors

Materials that have conductivities between those of metals and insulators are semiconductors. Semiconductors can be classified in two general groups that one of which is the elemental semiconductor materials, formed from group IV elements in the periodic table, and the compound semiconductor materials that composed of two or more elements, majority of which are composed of particular combinations of group III and group V elements. Also semiconductors can be composed of group II and group VI elements (Neamen, 2003). A section of periodic table related with semiconductors is shown in Figure 2.1.

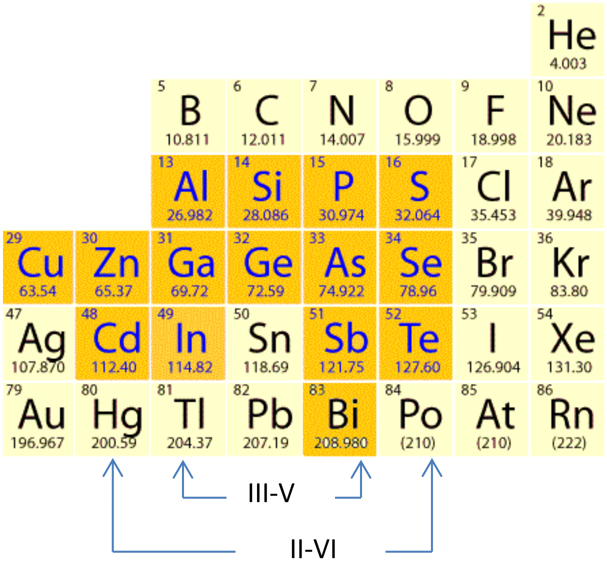

Figure 2.1: A section of the Periodic Table showing the elements involved in the formation of semiconductors. More common semiconductors are colored in yellow.

Examples of elemental semiconductors are silicon, germanium, etc. Silicon and germanium is commonly used elemental semiconductors especially in integrated circuits. Each of elemental semiconductors adopts the diamond cubic structure (Figure 2.2). Also, they have indirect band gap (Kittel, 2004).

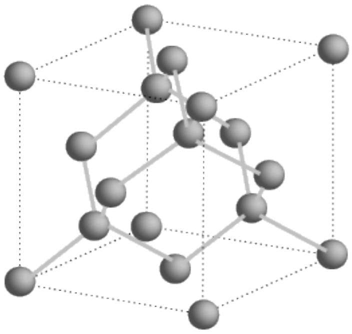

Figure 2.2: Crystal structure of silicon and germanium (Kittel, 2004).

Compound semiconductors can be categorized as binaries (III- V's, II-VI's, etc.) and alloy semiconductors such as ternaries, quarternaries and more than four element compound semiconductors. Most commonly used binary compound semiconductors are GaAs, AlAs, ZnS etc. The bonding becomes partly ionic for III- V compounds because of electronic charge transfer from the group III atom to group V atom. Semiconductor properties changes with ionicity. It enhances Coulomb interaction between the ions and the energy of primary gap in the electronic band structure as well. Due to high ionicity, most of the II-VI compound semiconductors' band gap is larger than 1 eV. Although large band gap II-VI's have potential applications for lasers, the smaller band gap II-VI's are significant materials for the production of infrared detectors (Yu and Cardona, 2010). Producing ability of layered structures which is provided material properties (such as band gap, band offsets, reflective index and transport properties) change that is provided a great flexibility design of devices. It is demonstrated schematically in the graph of band versus lattice constant for semiconductors in Figure 2.3.

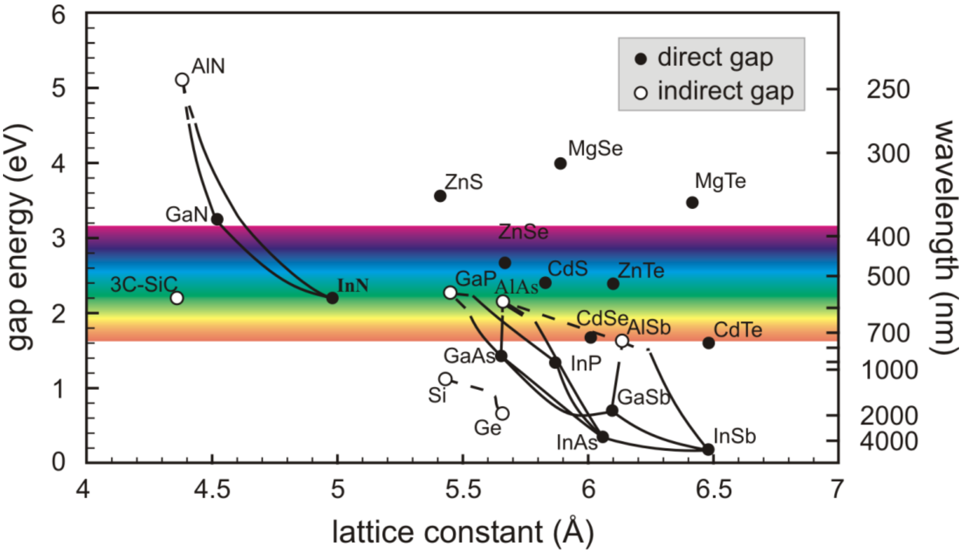

Figure 2.3: Band gap versus lattice constant for semiconductors (Ibach and Lüth, 2003).

The diamond lattice is the most common crystal structure among usually used semiconductors. In addition, many compound semiconductors such as Gallium Arsenide (GaAs) generally show the zinc blende crystal structure, and change in material properties by changing composition results from alloying the III-V semiconductors. The arsenides, phosphides and antimonides all show zinc blende structures (Figure 2.4). Contrary, the nitrides show a wurtzite structures (Figure 2.5).

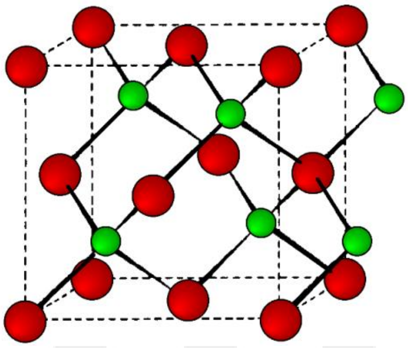

Figure 2.4: Zinc blende (ZnS) lattice structure (Barron, 2016).

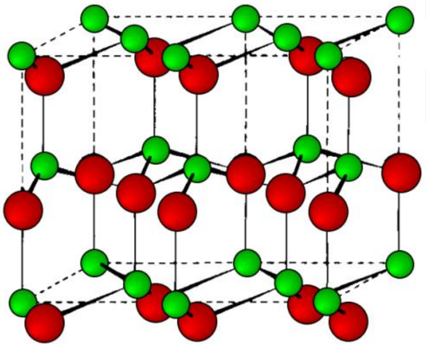

Figure 2.5: Wurtzite lattice structure (Barron, 2016).

Most binary compounds have direct band gap and comprise all wide range of wavelengths from ultraviolet (UV) to infrared (IR) can be covered. Ternary alloys are not compounds and there are two selection of III- V examples

$$A_{III(1-x)}B_{III(x)}C_{V}\ \{=[A_{III}C_{V}]_{(1-x)}+[B_{III}C_{V}]_{(x)}\}$$

$$A_{III}B_{V(1-y)}C_{V(y)}\quad \{=[A_{III}B_{V}]_{(1-y)}+[A_{III}C_{V}]_{(y)}\} \qquad (5)$$

Our structure represents ternary alloys and we can achieve to a consistent range of band gaps. Selection of material in this process needs to consider lattice parameters of materials which should be close each other due to low mismatch between the layers that results in high material quality.

2.3 Crystal Structure of GaAs and $GaAs_{1-x}Bi_x$

GaAs crystal is a cubic sphalerite or zincblende structure. The origin of the lattice consists of one GaAs molecule in the traditional basis. The crystal can also examine as two FCC lattices (Blakemore, 1982). The crystal structure is demostrated below in Figure 2.6. Ga atoms are demostrated in black while As atoms are demonstrated in red. The lattice consist of 14 Ga atoms and 4 As atoms.

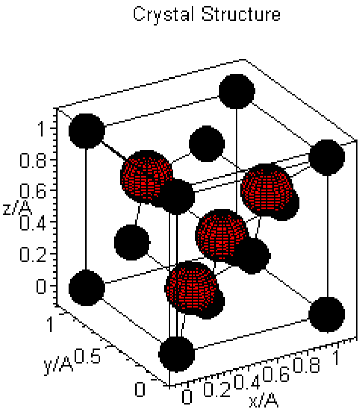

Figure 2.6: Face centered cubic unit cell of GaAs (Blakemore, 1982).

In Figure 2.7, it is shown that crystal conversion of zinc blende $GaAs_{1-x}Bi_x$ which is formed by addition of Bi atoms in GaAs.

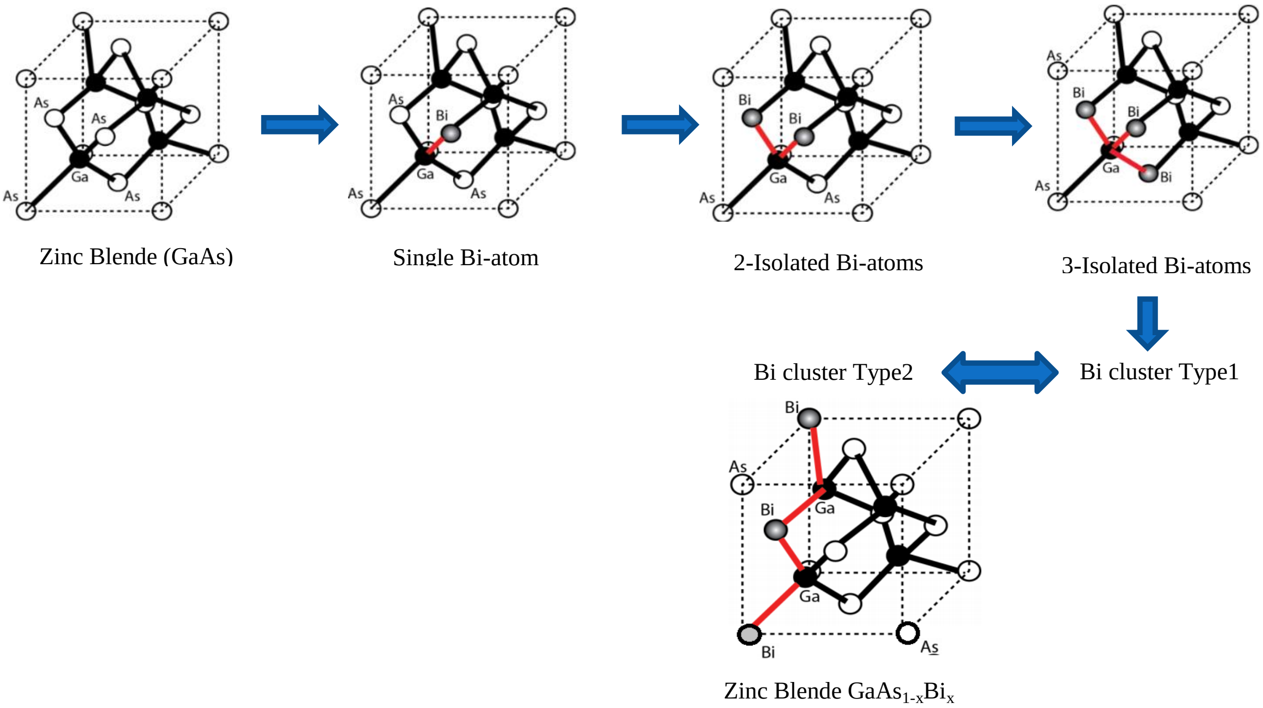

Zinc Blende (GaAs)

Single Bi-atom

2-Isolated Bi-atoms

3-Isolated Bi-atoms

Zinc Blende $GaAs_{1-x}Bi_x$

Figure 2.7: Crystal conversion of Zinc Blende $GaAs_{1-x}Bi_x$

2.4 Material Parameters of III-Vs

III-Vs are polar crystals because of the deficiency of a symmetry center along the c-axis that incline to lots of functional properties such as pyroelectricity, piezoelectricity and nonlinear opticality (Li, 1993). As well as, they can be used to function in high temperatures and many device applications due to their chemical and physical stability. As a result of high chemical bonding which is originated from the big variation in electronegativity between the group III and group V that provides considerably good thermal conductivity.

Table 2.1 Properties of Gallium, Arsenic and Bizmuth (Wolfram Mathematica, 2016)

Properties	Gallium (Ga)	Arsenic (As)	Bizmuth (Bi)
Atomic number	31	33	83
Atomic weight	69.72	74.92	208.98
Atomic radius	136 pm	114 pm	143 pm
Lattice constant	451.97 pm	375.9 pm	667.4 pm
Crystal structure	Base Centered Orthorhombic	Simple Trigonal	Base Centered Monoclinic
Density	6.09 (g/cm)^3	5.727 (g/cm)^3	9.78 (g/cm)^3
Melting point	29.76 °C	817 °C	271.3 °C
Specific heat	371 J/(kg K)	328 J/(kg K)	122 J/(kg K)
Thermal conductivity	29 W/(m K)	50 W/(m K)	8 W/(m K)
Thermal expansion	0.00012 K^{-1}	N/A	0.0000134 K^{-1}
Speed of sound	2740 m/s	N/A	1790 m/s
Electrical type	Conductor	Conductor	Conductor
Electrical conductivity	7.1×10^6 S/m	3.3×10^6 S/m	7.7×105 S/m
Resistivity	1.4×10^{-7} m Ω	3×10^{-7} m Ω	1.3×10-6 m Ω
Superconducting point	1.083	N/A	N/A
Valence electron	3	5	5
Electronegativity	1.81	2.18	2.02
ElectronAffinity	0.2995 eV	0.8083 eV	1,8969 eV
Ionization energy	5.9885 eV	9.8148 eV	88,608 eV

Magnetic type	Diamagnetic	Diamagnetic	Diamagnetic

2.5 Band Structure of Semiconductors

Schrödinger equation solution for electrons is provided energy against effective momentum relation which is named the band structure of the semiconductor. All semiconductors have its own proper band structure. The knowledge of semiconductor device needs to understand of the band structure in both the conduction band and the valence band (Sing, 2003). Semiconductor materials divided in two groups with regard to band structure.

2.5.1 Direct and indirect band gap semiconductors

Materials for which maximum of valence band and minimum of conduction band lie on the same value of k, called direct band gap materials. Most semiconductor valence band maximum arise from at $k = 0$. A characteristic band structure of a semiconductor is displayed in Figure 2.8. Two distinct $E - k$ curves near the valence band are observed. These curves (bands) are labeled I and II in Fig. 2.9 and are called the heavy hole (HH) and light hole (LH), respectively.

Materials that maximum of valence band minimum of conduction band does not take place at same value of k is called indirect band materials, such as Si, Ge, AlAs, etc.

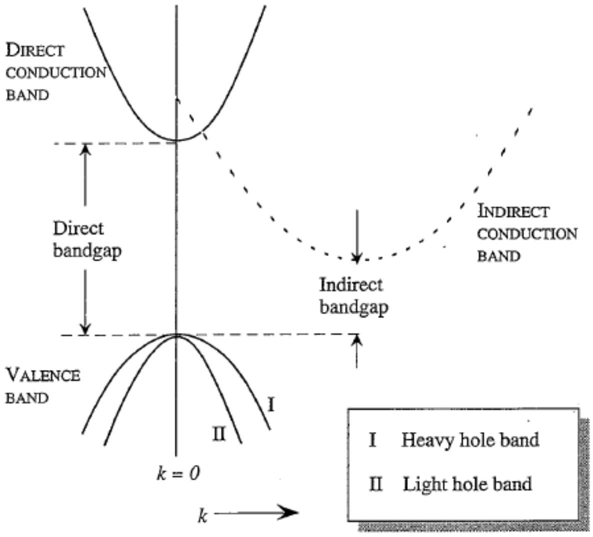

Figure 2.8: Schematic illustration of direct and indirect band gap semiconductor.

Because of level of the band edges in the valence band and the conduction band, direct band gap semiconductors have a strong interaction with light while indirect band gap semiconductors have comparatively weak interaction. This is an outcome of the law of momentum conservation. When the electron is moved from the top of the valence band to the bottom of the conduction band, it moves vertically in the over empty sites in the conduction band so momentum does not change and it is conserved. Also, the energy is conserved due to momentum conservation.

If the k-vector is the same as crystal momentum, for direct band gap semiconductors, the electron can directly emit a photon and

$$\vec{k}(photon) = \overrightarrow{k_e} \tag{6}$$

$$E = \hbar w_{photon} \tag{7}$$

If the k-vector is not same as crystal momentum, for indirect band gap semiconductors, the electron cannot directly emit a photon due to it have to pass straight the intermediate state and its momentum is transferred to the crystal lattice by phonons so the process have to include emission or absorption of a phonon.

$$\vec{k}(photon) = \overrightarrow{k_e} + \vec{k}(phonon) \tag{8}$$

$$E = E_g + \hbar w_{phonon} \tag{9}$$

where E is energy of photon, E_g is energy band gap, $\vec{k}(photon)$, $\vec{k}_e$ and $\vec{k}(phonon)$ are a wavelength of photon, electron and phonon, respectively. ħ is the Planck constant divided by 2π and frequency of photon and phonon is described as w_{photon} and w_{phonon}, respectively.

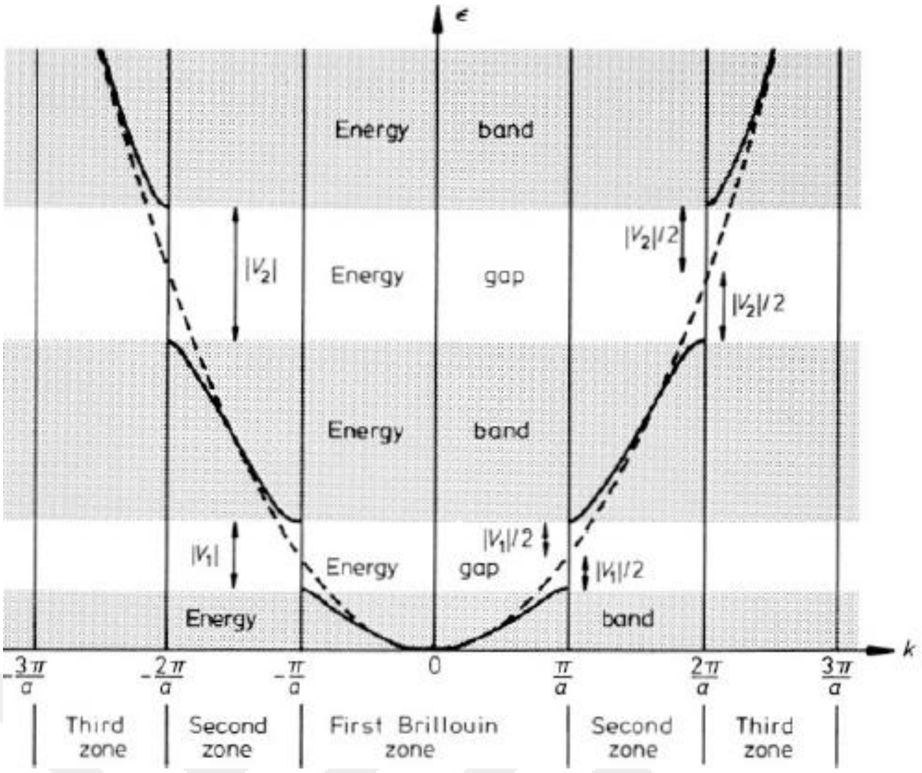

Figure 2.9: Schematic illustration of Brillouin Zones (Hook and Hall, 1991)

In Figure 2.9, it is shown that the k axis intrinsically separate into regions which is called Brillouin zones with the influence of periodic lattice potential on the electron states (Hook and Hall, 1991). This zones effects the electron mass and the new mass is called effective mass (m^*). The electron behaves like it had this mass due to electron reaction to the external world forces. In the first Brillouin zone m^* is positive, in second Brillouin zone m^* is negative as can be seen from Equation (11) and (12).

$$E = \frac{\hbar^2 k^2}{2m} \tag{10}$$

$$\frac{dE}{dk} = \frac{\hbar^2 k}{m} \tag{11}$$

$$\frac{d^2E}{dk^2} = \frac{\hbar^2}{m} \tag{12}$$

$$m^* = \hbar^2 (\frac{d^2E}{dk^2})^{-1} \tag{13}$$

The electron effective mass in conduction band has strongly effected on the value of the band gap. If the band gap is small, mass is small, as demonstrated in Fig. 2.10 (Sing, 2003).

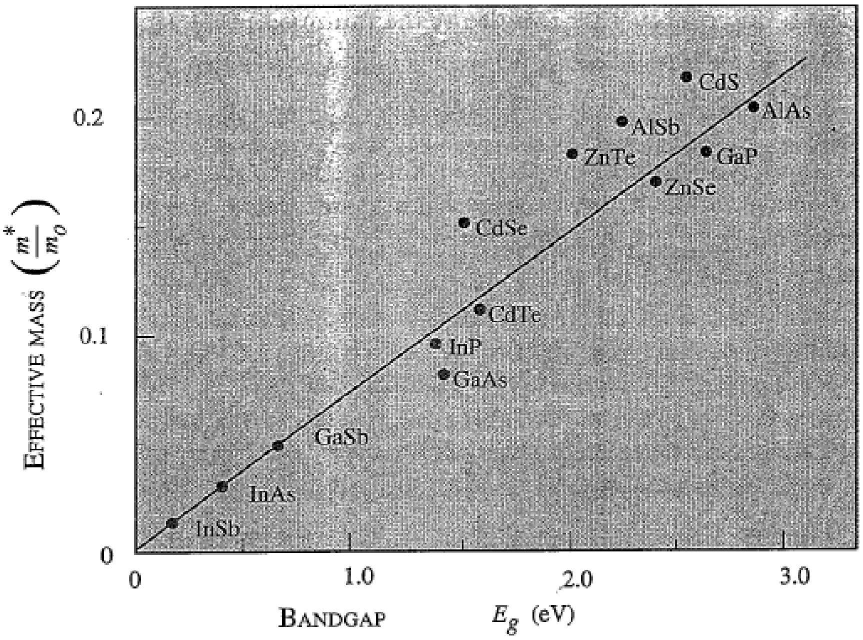

Figure 2.10: Conduction-band electron effective mass m^* versus band gap energy (E_g) for various compound semiconductors (Sing J, 2003).

2.6 Optical Properties of GaAs and GaAs$_{1-x}$Bi$_x$ Alloys

GaAs and GaAs$_{1-x}$Bi$_x$ are direct band gap compound semiconductors. The introduction of small concentration bismuth (Bi) in GaAs reveals the band gap reduction that makes favorable materials system for bismuth-based long wavelength optoelectronic devices such as IR detector, LED, Laser, etc. (Tixier et al.,2003; Francoeur et al. 2003; Huang, 2005). Also, for wireless communication systems, information transfer via the fiber optic cable with minimal loss depends on laser wavelength that have to be between 1300 nm and 1550 nm as given in Figure 2.11.

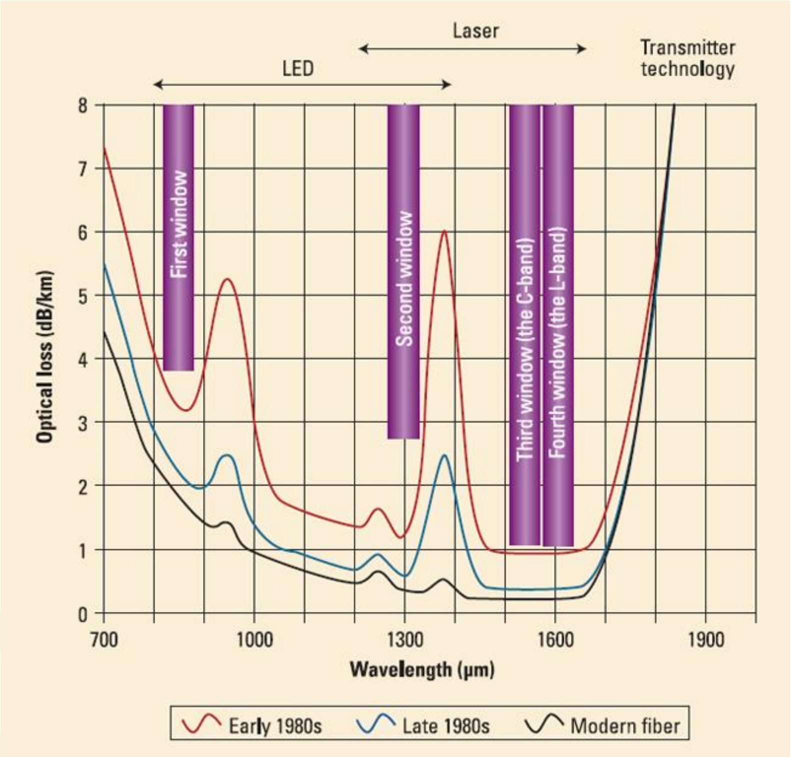

Figure 2.11: Optical loss versus wavelength (Broadcast Engineering)

The incorporation of small amounts of bismide in GaAs only slightly affects the crystal structure of GaAs while the band gap changes dramatically that make sense to use small amounts of bismide in GaAs for large changes in optoelectronic properties. The ability of large changes in optoelectronic properties make GaAs$_{1-x}$Bi$_x$/GaAs alloys preferred materials in family of III-Vs compound semiconductors.

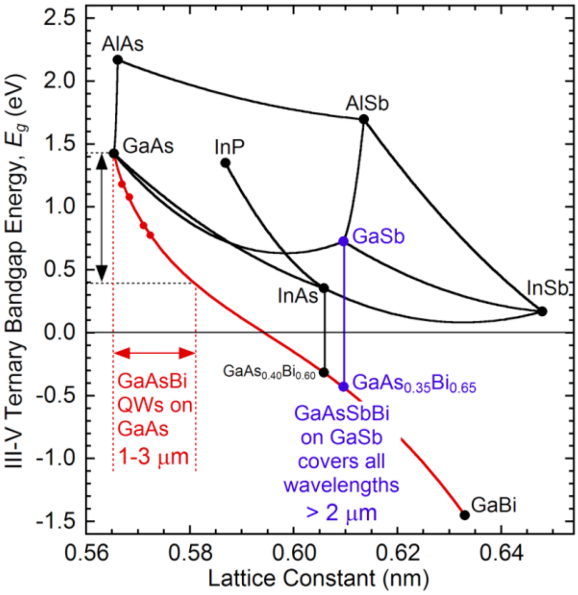

Figure 2.12: Band gap versus lattice constant for various III-V ternary semiconductors, including GaAs/GaAsBi (Shane Johnson, ASU)

The addition of small amount of Bismuth (Bi) atom into GaAs causes a wide band gap reduction. In general, replacement of a semiconductor element with one of smaller ionic radius of element is expected that increment of band gap. However, they observed exactly the opposite. Introducing a small amount of bismuth to GaAs lead to a great red shift rather than blue shift (Steele, 2016).

The band gaps versus lattice constant for various III-V ternary semiconductor materials shown in Figure 2.12. The lines combining the constituents and components forms the band gaps of ternary alloys. $GaAs_{1-x}Bi_x$ is demonstrated by the line connecting GaAs and GaBi where the amount of Bi increases in the alloy as you follow the line from pure GaAs to pure GaBi.

The band gap of semiconductor alloy directly depends on the constituent elements and the electron-phonon interaction. It is possible to change the consequent material band gap by the combination of three or more elements as shown in Fig. 2.12. In the following section, some effects of alloying in III-V semiconductor materials will be discussed.

The lattice parameter of an alloy can be estimated by a linear function of the composition, usually known as Vegard's law (Vegard, 1921).

$$a^{A_{1-x}B_x}(x) = xa^B + (1-x)a^A \tag{14}$$

Where the superscripts A and B designate the constituent end-members. Values of the parameter and band gap for common III-V semiconductors and their respective band gap energies given in Table 2.2.

Table 2.2 Lattice parameter and band gap of common III-V semiconductor materials (Adachi,1992)

III-V Alloy	**GaAs**	**GaBi**	**InAs**	**GaP**	**AlAs**	**InP**	**GaN**
Lattice parameter,$\dot{A}$	5.65	6.33	6.06	5.45	5.66	5.87	4.50
Band gap at 300 K, eV	1.42	-1.45	0.359	2.76	3.01	1.35	3.23

The majority of experiments, such as photoluminescence, X-ray spectroscopy, Raman spectroscopy, have been performed on $GaAs_{1-x}Bi_x$/GaAs alloys so as to clear up the disagreement about the true band gap energy. The low band gap of $GaAs_{1-x}Bi_x$/GaAs alloys is accelerated the research on the combination of GaAs and GaBi binary alloys. From the day forward, the small number of publications related to $GaAs_{1-x}Bi_x$/GaAs research have been published but it is raising day by day. Experimental data and theoretical research data based on recently grown, high quality $GaAs_{1-x}Bi_x/GaAs$ alloys has superior material properties for instance small effective mass, large electron mobility, and a small direct band gap.

2.7 Substrates

The improvement of a technology based on the III-Vs, mainly GaAs and $GaAs_{1-x}Bi_x/GaAs$ alloys is restricted by principle problems such as the low dissociation temperature of Bi (~271.3 °C), difference in lattice constants, thermal expansion coefficients and physical properties between $GaAs_{1-x}Bi_x/GaAs$ alloys and a suitable GaAs substrate. Until today, GaAs which grown on (100) direction is used as a suitable substrate for $GaAs_{1-x}Bi_x/GaAs$ alloys. However, in this work, we studied on GaAs substrates that grown on (100) and (311) B direction, as well. Also, lattice mismatch between GaAs and GaBi forms a high degree of strain that affects the mobility of electrons negatively. Besides, the high mismatch in lattice constants is the reason of high dislocation densities usually exciting in GaBi. High dislocation densities give rise to scattering that limits the carrier mobility so GaAs substrate has been proposed to reduce the mismatch.

2.8 Low Dimensional Structures

A low-dimensional electron system, which is one or more special dimensions are the small enough to limit the quantum mechanical wavefunction of electrons involved inside from exploring the full three dimensions of the world (Anonymous, 2016). Low dimensional systems that have received tremendous attention since then twenty years improved by permanent dramatic discoveries besides have a big potential for new electronic device applications. These systems have clarified the tough questions of how defects, such as impurities, and electron-electron interaction influence a quantum system. However, it is still a problem to understand the combined effects of defects and electron-electron interaction of a quantum system (Geller, 2001).

Notable progress in epitaxial growth techniques, such as Molecular Beam Epitaxy (MBE), Plasma Assisted Molecular Beam Epitaxy (RF-MBE), Metal-Organic Vapour Epitaxy (MOVPE), is provided the growth of extremely thin layers of semiconductors that ensure the confinement of electrons with accurate atomic dimensions result in substantial control of subband energies. By means of advanced epitaxial growth techniques, it is currently possible to squeeze the electronic wave function in one, two or the three spatial dimensions in solid state devices that providing the movement of carriers can be confined in the growth direction of crystal (Anonymous, 2016). This leads quantum phenomena. The conduction and valance bands are splitting into the discrete energy levels result from confinement of either electron or hole that the density of states is quantized into discrete energy states as is illustrated in Figure 2.13 (Bruce, 1986).

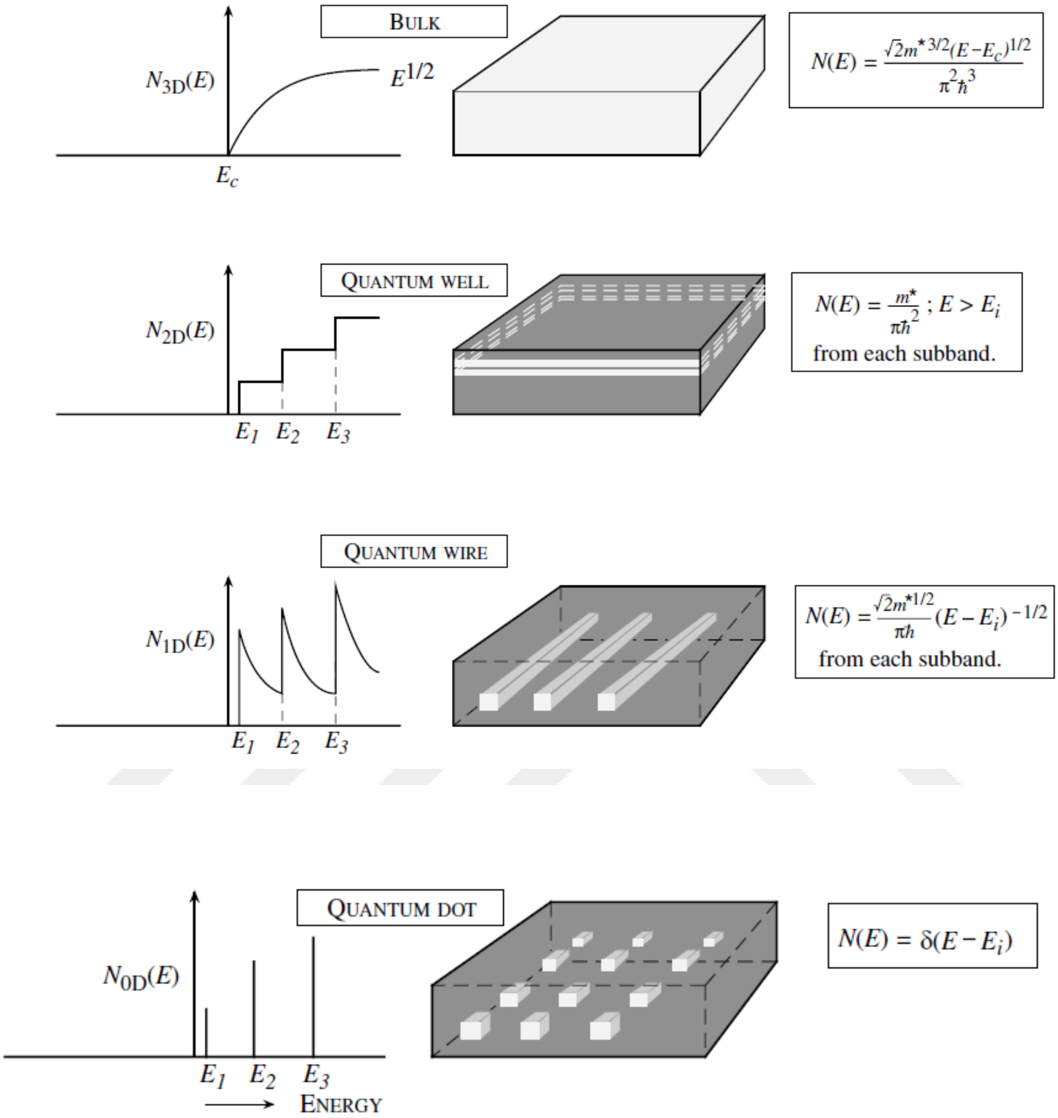

Figure 2.13: Schematics of the density of states as a function of dimensionality (Sing, 2003).

As a consequence, low dimensional structures properties show perfect progress in device efficiency than bulk materials. In general, these properties are optical, electric and magnetic properties which define applications to be used. The applications which wouldn't be without quantum phenomena are quantum computing, QD lasers, Stark effect modulators, resonant tunnelling diodes, etc. (Singh, 2003; See and Paul, 2001; Maximov et al., 2000; Grundmann, 1999).

2.8.1 Two dimensional systems

Two dimensional (2D) electronic system looks like a thin plate of confined electrons (Fig 2.14) in one dimension (generally along the growth direction) meantime their movement is free the other two dimensions. Electrons are free to move on the surface in the three directions of space (Joco, 2008). Quantized energy levels for movement of electrons in confinement direction result from strict confinement of electrons in one direction.

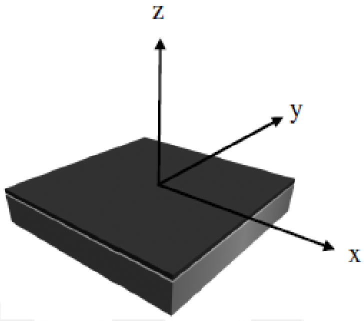

Figure 2.14: Illustration of a two dimensional system localization in the real space. The dark colored plane shows the electron confinement along the arbitrarily chosen xy plane (Joco, 2008).

Dispersion relation for two dimensions is calculated and described as:

$$n = \int_{E_c}^{\infty} N_e(E) f(E) dE \tag{15}$$

$$n = \frac{m^*}{\pi\hbar^2}\int_{E_c}^{\infty}\frac{(E-E_c)}{exp\left(\frac{E-E_F}{k_BT}\right)+1}dE \tag{16}$$

$$n = \frac{m^*}{\pi\hbar^2} exp(\frac{E_F}{k_BT}) \int_{E_c}^{\infty}(E-E_c)^{\frac{1}{2}} exp(-\frac{E}{k_BT})\, dE \tag{17}$$

$$E = E(k) = E_g + \frac{h^2}{2m}\,(k_x^2 + k_y^2) \tag{18}$$

where $N_e(E)$ is density of states of electron and Fermi fuction is defined as $f(E)$, E_c is energy of conduction band, E_F is Fermi energy, ħ is a Planck constant divided by 2π, k_B is Boltzmann constant, T is temperature, m^* is effective mass. Only on the z direction electron delocalization exists in the k-space.

CHAPTER 3

3. EXPERIMENTAL TECHNIQUES

3.1 Introduction

The following chapter discusses all experimental techniques used in this work. The techniques experienced to assess the grown samples and the methods via their optical, structural and electrical properties were examined. Experimental techniques includes details about experimental set ups, practical procedures and some theoretical background of techniques. The chapter is divided into four sections, introduction, material growth techniques and structural characterization, respectively.

3.2 Material Growth Techniques

The following section will briefly review the main growth techniques. There are two main crystal growth techniques: Bulk crystal growth and epitaxial crystal growth. Each of these epitaxial processes has distinct advantages and disadvantages discussed following topics.

3.2.1 Bulk crystal growth

Bulk crystal growth techniques are utilized exclusively for the manufacture of substrates in which the devices are ultimately manufactured. The purpose of this technique is to produce a single crystal boules with large diameters and with few defects (Singh, 2003). Czochralski (CZ) technique is used the growth of boules to make up the crystal. The melting charge is held in a vertical crucible in CZ technique shown in Figure 3.1. A seed crystal is pulled down into the melt and slowly retracted. As the heat from the melt flows upward from the seed, this induces cooling of melt surface and then the crystal starts to grow.

Si, GaAs, and InP can be produced by using the CZ technique. For GaAs, CZ technique has some problems due to As has very high pressure and the chamber must endure such pressures but also the As leave the melt and become dense on the sidewalls (Singh, 2003). Because of this reasons, this growth technique is not preferable for GaAs materials which will be used especially in electrical and optical applications.

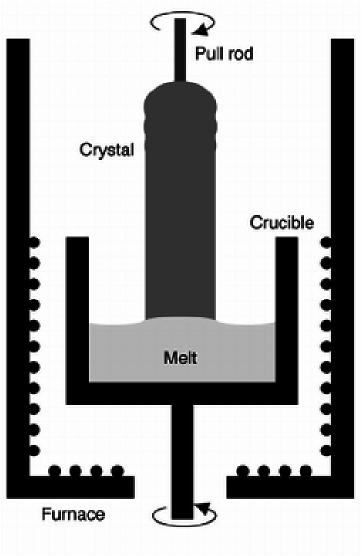

Figure 3.1: Schematic of bulk crystal growth (CZ technique) system (Yeckel and Derby, 2004)

3.2.2 Epitaxial crystal growth

Bulk crystals are grown and after sliced into substrates or wafer about 250 μm thick then polished and used for growth of epitaxial layers. These epitaxial layers are used for growing all active devices. As a consequence epitaxial growth techniques are really important due to slow growth rate of these epitaxial layers ensures controlling implicitly the dimensions in the growth direction. For the growth of epitaxial layers, various epitaxial growth techniques have been used such as Liquid Phase Epitaxy (LPE), Vapor Phase Epitaxy (VPE), Metal Organic Chemical Vapor Deposition (MOCVD) and Molecular Beam Epitaxy (MBE).

3.2.2.1 Liquid Phase Epitaxy (LPE)

LPE is a comparatively basic and multiple method to grow thin layers of III-V and IV-VI compounds for material investigations and device applications such as laser diodes, integrated bipolar transistor-laser circuits, multi-quantum well lasers that have made LPE technique a unique among the other epitaxial growth technique (Kuphal, 1991). It is less expensive technique compared to MBE or MOCVD, but it presents less control when growing heterostructures (Owens, 2012).

The process is frequently used for alloy growth in which the growth follows the equilibrium solid-liquid phase diagram. The alloy composition can be controlled by both control of the liquid composition and the temperature. Even so, heterostructures where interface is 10-20 $\AA$ can be grown by LPE with sliding the boat over sequenced ‘puddles’ of different semiconductors (Singh, 2003).

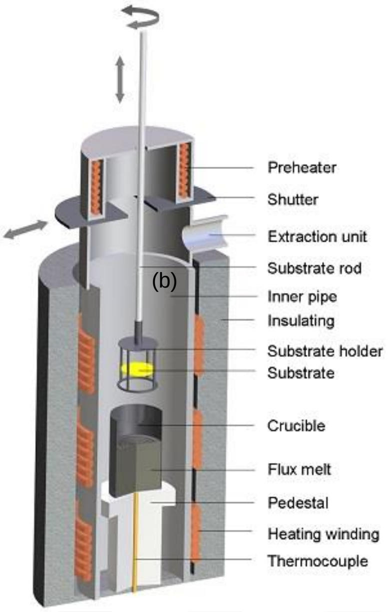

Figure 3.2: A schematic illustration of the LPE growth for general materials (Innovent Technologieentwicklung Jena Catalog)

3.2.2.2 Vapor Phase Epitaxy (VPE)

Vapor phase epitaxy technique provides growing by vaporizing source material for III-V compounds that inorganic or organic materials that react with the other materials to form the compound semiconductors on the substrate. Growth is controlled with the partial pressures of each of components of the source material (Rahman and Hasan, 2016). Figure 3.3 shows the VPE system for epitaxial growth of III-V compound. There are three different classification of reactor forms of vapor phase epitaxial growth that is (a) horizontal reactor, (b) vertical reactor and (c) cylindrical reactor.

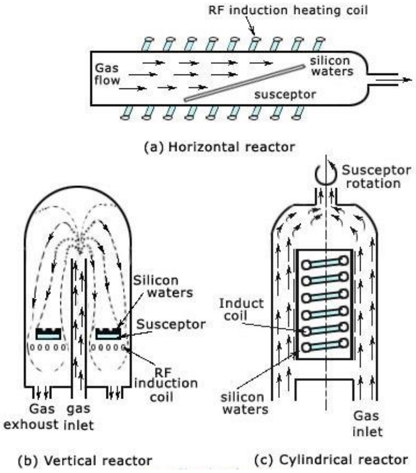

Figure 3.3: VPE growth reactors (VLSI, 2011).

3.2.2.3 Metal Organic Chemical Vapor Deposition (MOCVD)

MOCVD is other important growth technique extensively used for heteroepitaxy and especially for grow high-quality epitaxial III-N films. It was discovered by Manasevit in the late's 1960's (Manasevit, 1968). A schematic illustration of an MOCVD system is demonstrated in Figure 3.4.

The gases are used in MOCVD are complex molecules like Ga or As to create the crystal. Therefore, chemical reactions control the growth (Singh, 2003). For example, growing of GaAs needs to use triethyl gallium ($(CH_3)_3Ga$) and arsine (shown in Figure 3.4), the crystal growth reaction is

$$\mathrm{Ga(CH_3) + AsH_3 \leftrightarrow GaAs + 3CH_4} \tag{19}$$

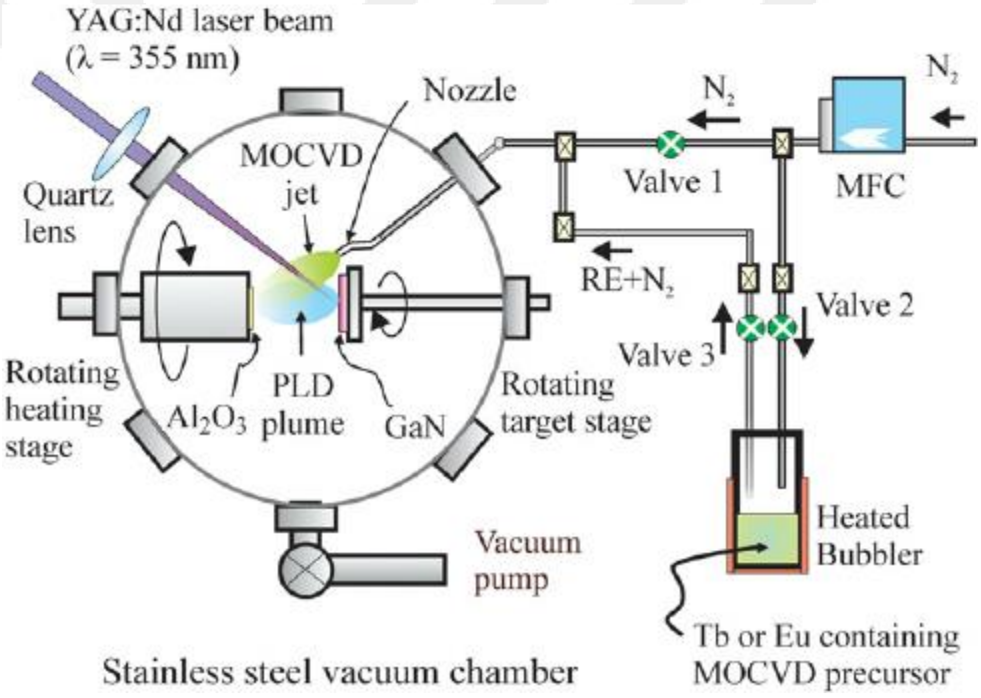

Figure 3.4: Schematic illustration of an MOCVD system (Lopez et al., 2008).

The metal organic source material are mixed with hydrogen carrier gas and transported over a heated substrate (GaAs) in a reactor. These sources resolve in a hot zone over the substrate while the group-III and group-V elements diffuse to the surface of the substrate. The vent line was refined with nitrogen and oxygen and purified with a passive cleaner to remove all impurities such as oxygen.

The advantage of the growth with MOCVD is regional area growth can be controlled laterally in temperature by chemical reactions besides laser assisted local area growth is also feasible for some materials is provided to manufacture new variety of device structures (Singh, 2003).

3.2.3 Molecular Beam Epitaxy (MBE)

The word epitaxy refers to growth of a crystal on a crystalline substrate that specifies its orientation. Generally, deposited film lattice parameter will be the same as those of the in-plane film in many applications. Therefore, when the deposited films material is similar to the substrate material that is called the homoepitaxy and deposited film's crystalline characteristics will be the same as those of substrate. Deposited films have slightly different optoelectronic properties than the substrate because of a small amount of impurities in a growth process. For example, the intentional addition of Bi in GaAs makes the material p-doped so the properties of last product (alloy) has controllable properties with addition of Bi (Beaton, 2011).

MBE is one of the most complicated and crucial epitaxial technique generally used in growing single crystals. Firstly, J.R. Arthur and A.Y. Choover grew GaAs-GaAs and GaAs-$Al_xGa_{1-x}As$ heterostructures by MBE in the late 1960s (Palping, 1980; Parker, 1985; Chang and Ploog, 1985; Cho, 1971; Arthur, 1968). An MBE system is performed under ultra-high vacuum conditions (UHV) where the background pressures are generally as low as $1x10^{-10}$ Torr by UHV chamber that separated by furnace surfaces (crucibles). Very high purity in the epilayer is provided by UVH conditions. Shutters, a substrate manipulator, some surface-analysis tools, and cryoshrouds enclosing the entire growth area to minimize the residual water vapour and carbon containing gases in the vacuum chamber during epitaxy are important parts of MBE. Ga, Bi and As are loaded in crucibles inside Knudsen cells. Molecular beams are generated by heating Knudsen effusion cells and diffused into a reaction chamber. The shutter is used for controlling the generated beams. Generated molecular beams travel in an UHV Chamber to hit on the heated substrate surface when the shutter is open and the pressure of the molecular beam is low ($\sim 10^{-6}$ Torr).

3.2.3.1 General principles of solid source-MBE

Effusion cells contain elements to be grown. The group III elements (Ga, In, Al) are introduced in the liquid form while group V elements (As, Bi, Sb) are used in the solid form. The amount of evaporated material is measured by beam flux. The growth rate is quantified by RHEED oscillations (Gunes, 2010). A general solid source MBE system and a schematic drawing of solid source MBE growth chamber is presented in Figure 3.5 and Figure 3.6, respectively.

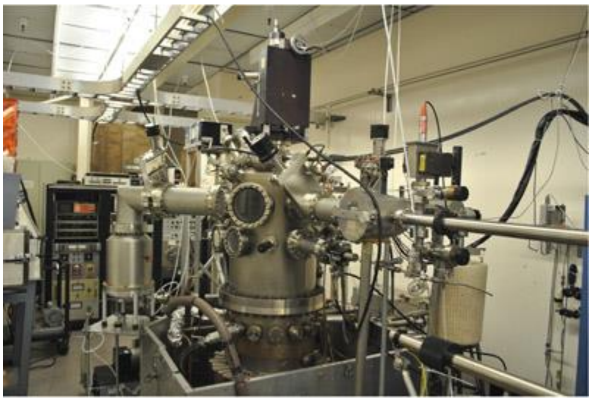

Figure 3.5: Solid source MBE system (Device Research Laboratory Catalog)

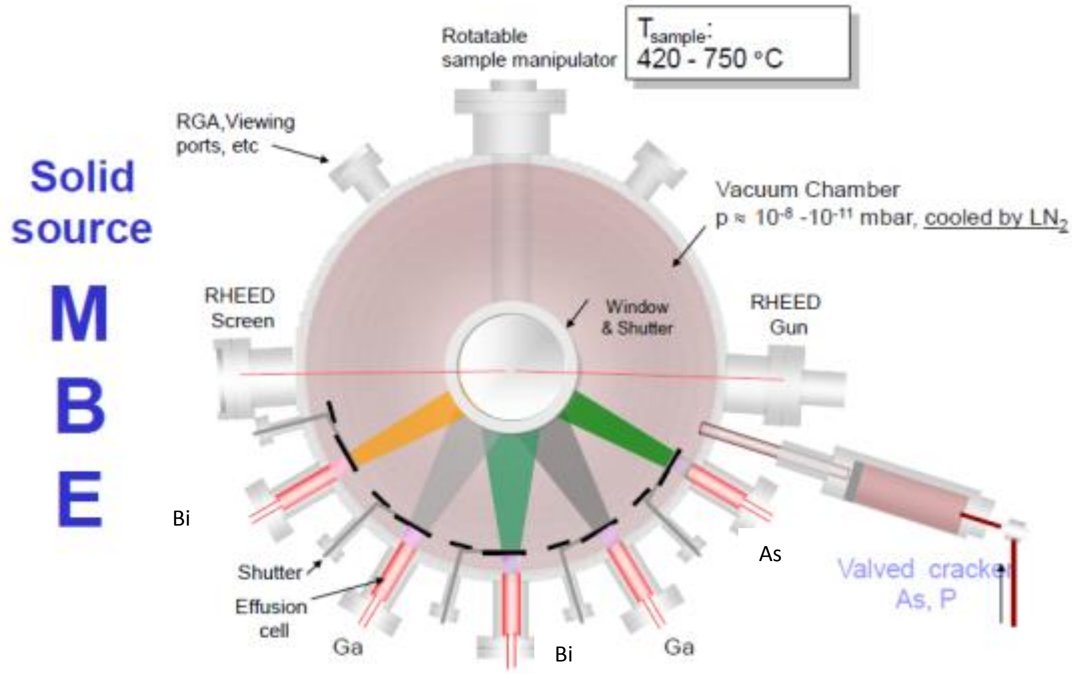

Figure 3.6: Solid source MBE growth chamber (Guina, 2009)

-Elements are introduced as solids.

-The substrate temperature is about: ~650 ^{0}C (GaAs)

-General growth rate is really slow and in the range of 0.3-1 $\mu m/h$ not permitting three-dimensional island formation but permitting monolayer by monolayer growth (Singh, 2001). During the growth, the substrate is generally rotated constant speed so as to get better uniformity of composition, dopant and thickness.

-For improving the vacuum and reducing contamination that arise from the substrates and hindering the atoms and molecules coming from the chamber walls, liquid N_2 is used for cooling the growth chamber walls.

Except for the growth chamber, in MBE system there are two UHV chambers: a buffer chamber and a load lock. The samples to be taken in and out of the UHV environment during maintaining the vacuum integrity of the other chambers by load lock. For preparation, cleaning, storage of samples and ratherly material characterization to be in the buffer chamber. The substrates are newly etched and heated to stay a close atomically clean surface is provided through UHV environment. Reflection high-energy electron diffraction (RHEED) is provided to use surface sensitive diagnostic techniques which require vacuum under favour of a unique advantage of UHV environment capability (Neave et al., 1983). RHEED gives information about surface morphology, surface reconstruction and growth rate by a high energy (generally 10-15 keV) electron beam generated by RHEED guns that directed on the sample surface a grazing angle of between 1^0 and 3^0. Surface-sensitive diffraction pattern is determined by the grazing incidence which the electron beam is scattered a few atomic layers into the crystal (Biasiol and Sorba, 2001). When the electrons are diffracted by the crystal structure of the sample in that case a surface-sensitive diffraction pattern is imaged on a phosphor screen that mounted opposite to the electron gun. By the time the sample is grown layer by layer, RHEED pattern oscillates with time and the period of oscillation accounts to the time needed to grow a monolayer as can be seen in Figure 3.7. Due to the coverage statically distributes over more and more layers and in the end a constant surface roughness is yielded, the magnitude of oscillations is quenched as the growth progress. Fundamental information about the surface geometry and chemistry can be seen with the RHEED pattern in Figure 3.7, for instance: spotty patterns indicate rough surface, sharp streaks indicate a smooth surface.

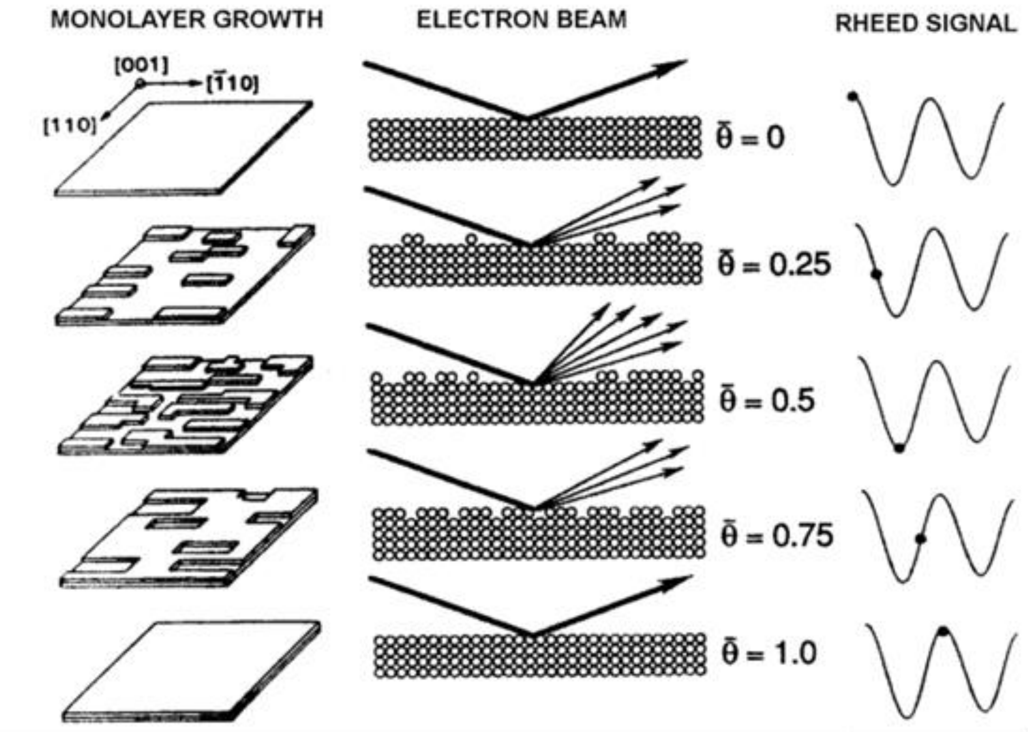

Figure 3.7: RHEED Intensity Oscillations (Neave et al., 1983).

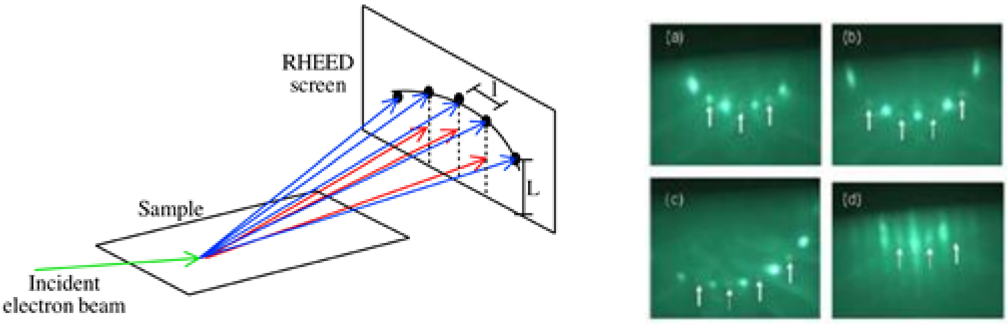

Figure 3.8: A typical RHEED pattern (Neave et al., 1983).

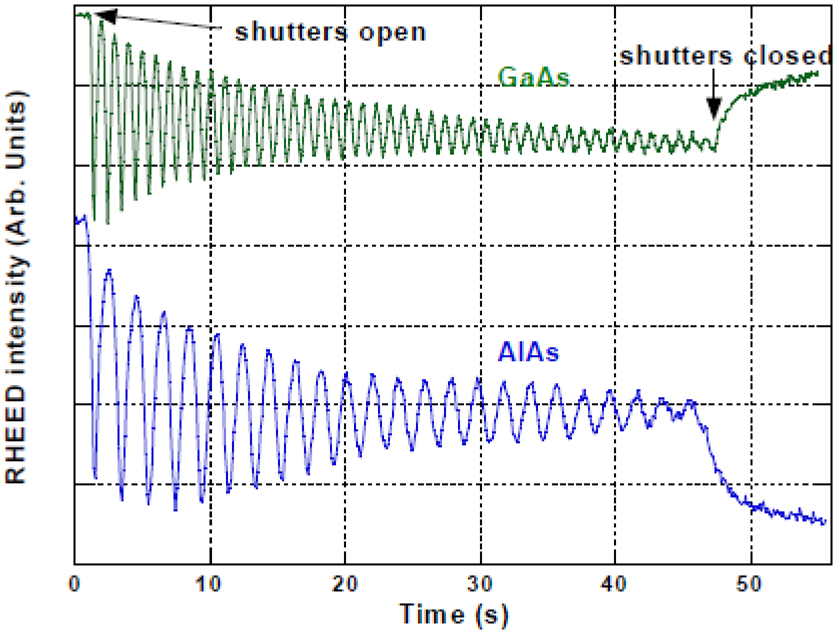

Figure 3.9: RHEED intensity oscillations of during GaAs and AlAs growth (Biasiol and Sorba, 2001).

3.3 Material Growth

The studied structures were grown on semi insulating GaAs (100) oriented substrates by MBE. The growth of GaAsBi QW samples started a 300 nm thick GaAs buffer layer at 580 °C then the growth temperature was declined to 315°C to improve the incorporation of Bi in the QW. Then a 10 nm thick GaAsBi QW layer was grown followed by a 50 nm GaAs cap layer grown at the same temperature (see Fig.3.10). The growth rate was 0.45µm/h for all layers. For efficient Bi incorporation, the atomic Ga/As flux ratio for the QW and cap layers was close to the stoichiometric value. The Bi concentration varied from 1% to 3%.

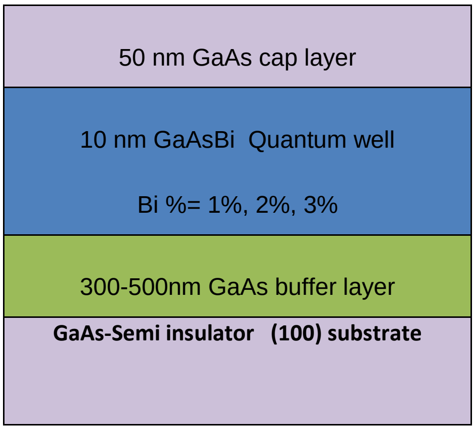

Figure 3.10: Layer structure of the investigated structures grown by MBE

3.4 Structural Characterization

Atomic Force Microscopy (AFM) and X-ray Diffraction (XRD) measurement techniques were performed to investigate the structural properties of the MBE grown samples. Surface morphology of GaAsBi QW samples was investigated by AFM; while XRD has been used to characterize crystallographic structure of samples. The mechanisms of AFM and XRD are explained below.

3.4.1 Atomic Force Microscopy (AFM)

Scanning Probe Microscopy (SPM) consist of a sharp probe with a cantilever which can scan across a surface and through the probe-sample interactions the surface morphologies are monitored on computer screen. AFM is known as Scanning Tunelling Microscopy as well. There are three main methods of AFM are Contact Mode, Non-contact Mode and Tapping Mode AFM which is conceived to characterize the surface morphology of bismuth containing compounds. Tapping mode AFM is provided higher lateral resolution on most samples. However, the only defect of tapping mode is partially slower scan speed compare to Contact Mode AFM (Roy, 2012).

3.4.1.1 Experimental set-up for AFM

Tapping mode AFM characterization has been performed for 5x5 scan size and for different scan directions. For controlling sample scanning and post data analysis Nanoscope software is used.

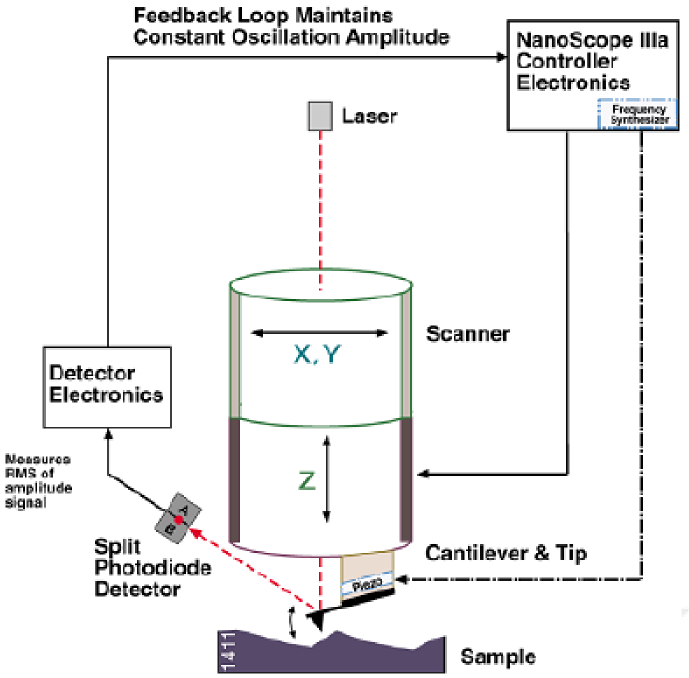

Figure 3.11: Schematic diagram of a Tapping Mode AFM with basic components (Roy, 2012).

Figure 3.11 shows the experimental set-up for tapping mode AFM with basic components, where a tip attached to the end of an oscillating cantilever thus the tip can scan across the sample surface. The resonant frequency of the oscillated cantilever follows amplitude, ranging from -10 nm to 10 nm. For keeping a constant RMS of the oscillation signal, a split photodiode detector is used and later the feedback loop maintains constant oscillation amplitude. Thanks to feedback loop maintain, a constant tip-sample is maintained during the scanning. So as to form the image of the sample surface, the vertical position of the scanner (i.e., each (x,y) data point) and the horizontal position of the scanner (i.e., each (z) data point) maintains a constant amplitude, which is stored by the computer (Roy, 2012).

3.4.2 High resolution X-ray diffraction (HRXRD)

X-ray diffraction (XRD) techniques are versatile means in the study of crystallographic structure of materials. A material is exposed to collimated beams of X-rays in XRD. When the X-rays interact with the atoms' electronic clouds each of the atoms re-radiating a spherical wave with the same frequency as the incident wave. Only if the atoms are arranged in a regular array, for example they form a crystalline structure, the spherical waves can structurally hinder in a few specific directions that determined by Bragg's law (equation 10).

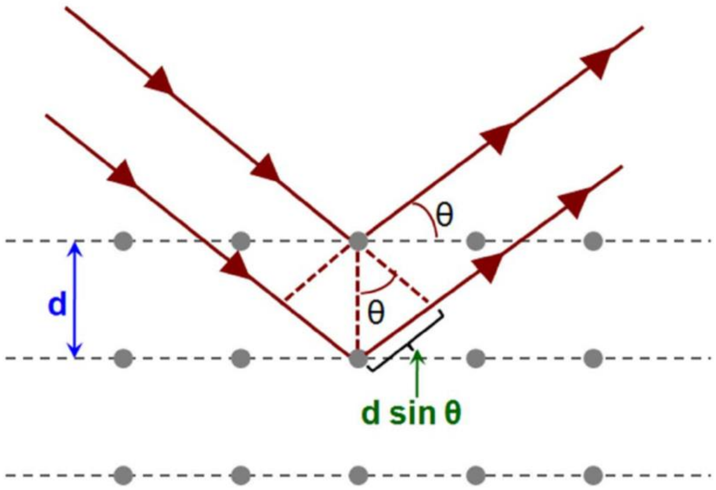

Figure 3.12: Proof demonstration of Bragg's law (Baskaran, 2010).

$$2d\ \sin\theta = n\lambda \tag{20}$$

Where, d is the spacing between the crystal lattice planes, θ is the incident angle with regarded to diffracting lattice plane, n is an integer and λ is the wavelength of the X-rays. A diffraction pattern can be seen when scanning along a range of incidence angles because of the X-ray wavelength being comparable to the lattice plane spacing.

The purpose of high resolution X-ray diffraction (HRXRD) is to specify slight deviations from the ideal crystal structure that would end up with a slight deviation in the diffraction maximum position (which referred as simply mismatch). The detection of these deviations is especially practical for the analysis of thin films as long as the epitaxial layers are generally slightly lattice mismatched from the substrate. For instance, if a thin epilayer has slight lattice mismatch from the substrate, it forms an additional diffraction peak next to the substrate diffraction maximum. By reason of proportionality of lattice mismatch with epilayers' composition or defect concentration can be determined certainly. The epilayers' thickness can be determined by analyzing the Pendellösung fringes around the secondary peak. If these features are destroyed, structural inhomogeneity or interfacial quality can be qualitatively measured by HRXRD. Also, relaxation of the epilayer can be quantatively measured by reciprocal space mapping (Hilska, 2016).

3.4.2.1 Experimental set-up for XRD

Double crystal X-ray rocking curve measurements were carried out by Panalytical X'Pert Pro MRD HRXRD system. The X-rays are created in a ceramic high power X-ray tube via a Cu anode that ensures Cu K-alpha radiation with a long line focus. For conditioning the X-ray beam, an X-ray mirror along with a four crystal Ge(220) monochromator are employed.

To control the beam dimensions, a crossed slits assembly is mounted to the end of the monochromator. For maximizing the incident X-ray intensity, the assembly slits were left fully open, thus the beam dimensions were specified by the mirror and monochromator apertures. When the beams heated the sample, the beam dimensions are roughly ~1.8 mm in width and ~14 mm in height. A proportional detector composing of a cylindirical chamber filled with a xenon/methane mixture collects the diffracted intensity. A narrow detection range of 12 arcseconds by having the diffracted beam undergo three Ge(220) reflections is provided by an analyzer (Hilska, 2016).

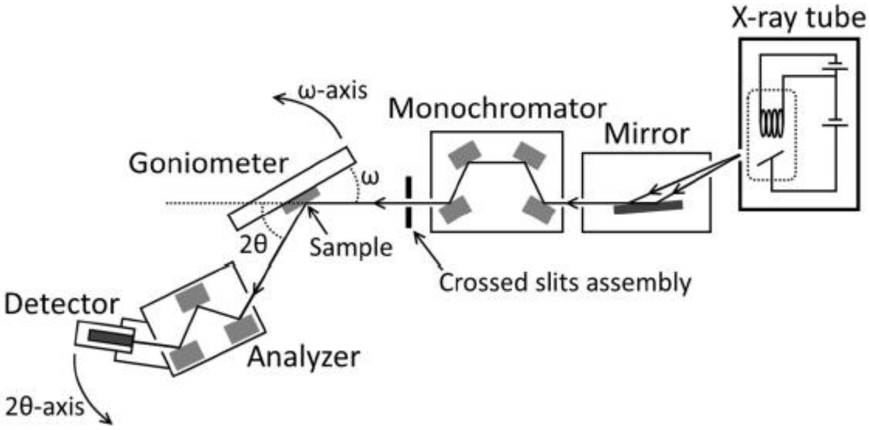

Figure 3.13: Schematic of the experimental setup showing the optical path of the X-ray beam (Hilska, 2016).

In this work, the HRXRD measurements are called $\omega - 2\theta$ triple-axis coupled scans. In these scans both of the ω- and 2θ- axis, which is shown in Figure 3.13, are rotated concurrently with the 2θ- axis being moved via twice the angular velocity. The mismatched Bragg peaks are observed for epilayers parallel to the substrate when using a symmetric scan (i.e. $\omega = \theta$). Particularly, the diffraction maximum corresponds to the GaAs (004) lattice planes are quantified over. This is because of high structure factor that governs the maximum diffraction intensity.

3.5 Optical Characterization

3.5.1 Photoluminescence spectroscopy (PL)

Photoluminescence (PL) spectroscopy is a technique for investigation of optical properties of semiconductors due to it is a contact-free and non-destructive technique. High-resilience materials can be investigated without any sample preparation because of no electrical contact requirement. The technique gives the information about impurity levels, defect detection and recombination process (radiative or non-radiative transitions) that present in semiconductors. For this reason, the purity and crystalline quality of semiconductors can be measured by this technique. The photons that have enough energy ($h\nu_{exc} > E_g$) are directed on the sample and the photons are absorbed and transfer its energy into the material producing electron-hole pairs. This process is named as photo-excitation. If the recombination is radiative, the photo produced non-equilibrium carriers recombine and consequently the great energy provided by the pump beam is distributed by the emission of light (Lyon, 1986). When the non-radiative transitions excited electrons, they lose their energy by thermalization by way of releasing acoustic or optical phonons. The electronic transitions observed in the semiconductors are illustrated in Figure 3.14 (Gunes, 2010).

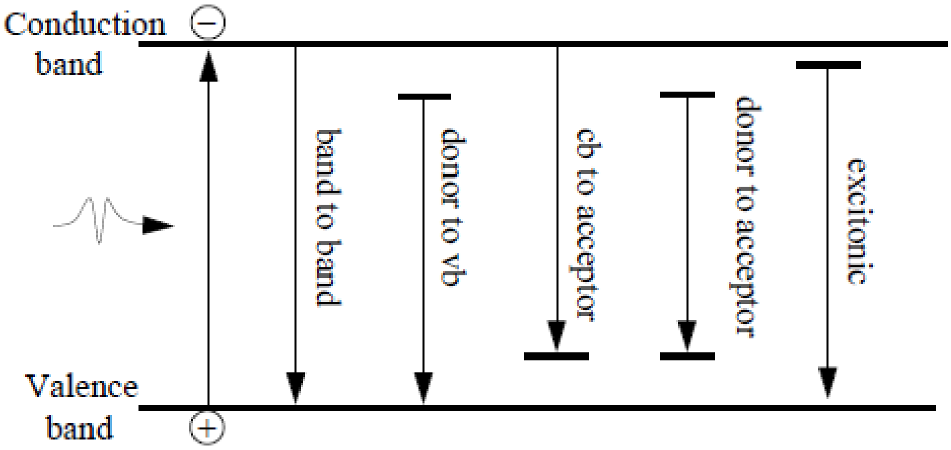

Figure 3.14: Possible radiative recombinations in semiconductors (Gunes, 2010).

The energy of emitted light bases on the difference in energy levels between the two electronic states that the transition between the excited state and the equilibrium state. The intensity of the emitted light is related with a relative contribution of the radiative process. Energy difference which is known as the band gap is between states in the conduction band and valence bands is the most extensive radiative transition in semiconductors (Stradling and Klipstein, 1990). If there is intentionally or unintentionally doping occurs, donor and acceptor levels can be incline to a radiative transitions such as donor to valence band (D^0,h) and conduction band to acceptor (e, A^0). Also, there are another important transitions that might take place at low temperatures are excitonic transitions in other words free and bound excitons. Electron-hole pairs namely excitons are bound by Coulomb interactions. Excitons are free to move in the crystal in the absence of any other interaction with other centers except from Coulomb interactions. These excitons are called free excitons. If excitons interacts with a neutral, ionized impurity, or some other defects in semiconductor lattice, they are called as bound excitons. These interactions seen as a sharp peak in the spectra. Energy of bound excitons which can be related with the emission energy is lower than the free excitons. The schematic illustration of radiative recombination with acceptors bound to holes in semiconductor is shown in Figure 3.15.

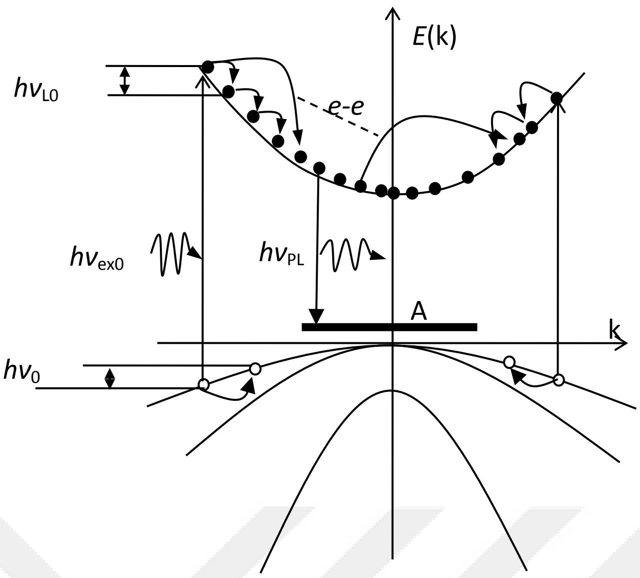

Figure 3.15: Mechanisms involved during PL emission (Gunes, 2010).

Defect, trap or impurity activation energies in the material can be determined by temperature dependent PL. Actually, every process regard to a recombination center is qualified by activation energy correlate to a certain temperature range. It is possible to calculate these activation energies by looking at the temperature dependent PL feature. Additionally, a variation of the semiconductor energy band gap as to Varshni's equation can be defined by a change in the lattice temperature (Varshni, 1967).

$$E_g(T) = E_0 - \frac{\alpha T^2}{T+\beta} \tag{21}$$

Where, $E_g(0)$ is the band gap energy of the material at $T = 0\,K$, while α and β are fitting parameters that are specific for each material, and they can be used to identify the composition of any compound.

3.5.1.1 Photoluminescence experimental set-up

The Photoluminescence measurements were performed on a Bruker Vertex 80 V Fourier transform infrared spectrometer. The PL spectra was excited using of 532 nm laser and collected by Silicon Avalanche Photodiode. The samples were cooled into a closed-cycle Helium cryostat.

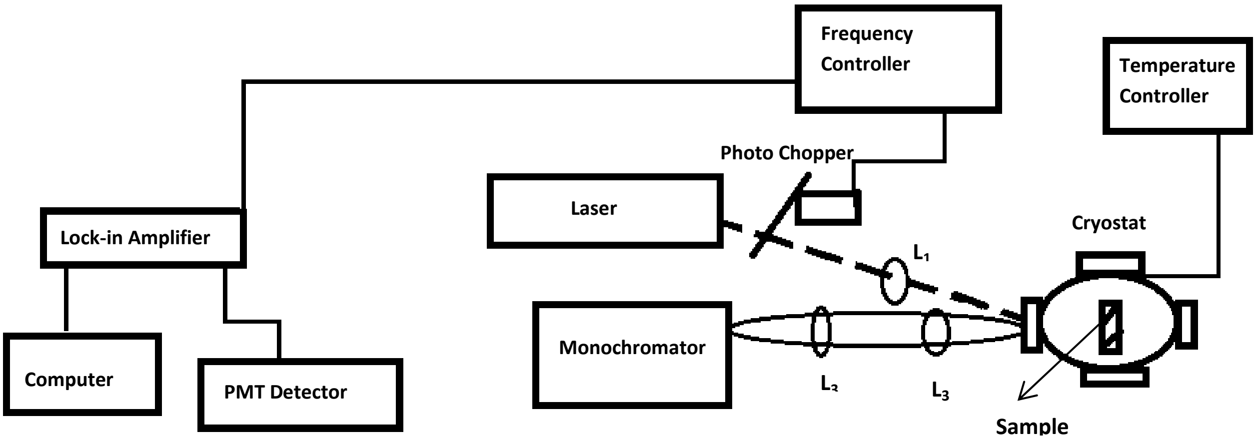

Figure 3.16: Experimental set-up for Photoluminescence

3.5.2 Raman spectroscopy

Raman Spectroscopy is a significant spectroscopic technique which is used to characterize materials. Because of it doesn’t need an electrical contact, it is a non-destructive technique. This technique ensures information about molecular vibrations which can be utilized for sample identification and quantitation. In 1930, Indian scientist C. V. Raman who won the Nobel Prize in Physics discovered Raman technique via using sunlight for a main excitation source and for creating a monochromatic light a narrow band photographic filter is used. These created monochromatic light was blocked by a crossed filter. Transversely scattered beams via materials were allied to the wavelength of the incident source and these beams also strongly polarized was discovered by C. V. Raman (Anderson and Dekker, 1971). Many physical and chemical properties of crystals were specified to compare the polarization of the Raman scattered light with regard to the crystal and the polarization of the laser light. Also, the low frequency excitations in solids such as, phonons (Bruesch, 1987), plasmons (Hayes and Loudon, 1978), magnons and superconducting gap excitations has been investigated before. What is more, the information about the crystal identification, crystal orientation, alloy composition (Saint-Cricq et al., 1987) , line shape and the polarization of the excitations (Hayes and Loudon, 1978), structural disorder, strain, imperfections and carrier concentration (Samson et al., 1992; Shen et al., 1985) can be defined by this technique.

3.5.2.1 The basis of the Raman effect

It is very practical technique to research lattice vibrations and their interactions with other excitations due to the technique is based on electron-phonon (lattice vibration) interactions. In this technique, the monochromatic light $(h\nu_0)$ is directed on a sample and detecting the scattered light as a consequence of interaction with the electron cloud and the bonds of the molecule. In Figure 3.17, the scattered light is investigated for its intensity I_s as a function of frequency v_s.

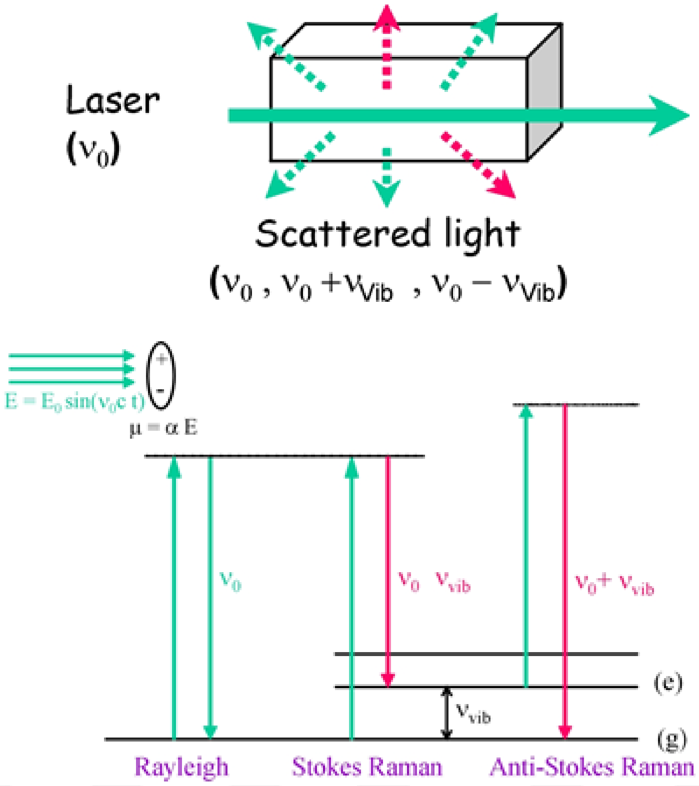

Figure 3.17: Energy level schema demonstrating the states included in Raman scattering (Gunes, 2010).

Where the intensity of light from a laser source is I_I, v_0 is frequency passes through the medium of volume (v) and it scattered in all directions which satisfies the law of conservation of momentum and energy. e and g represents 1^{st} excited vibrational and ground vibrational state, respectively. When the light is scattered elastically, the frequency of the reflected light stays identical to the incident light (v_0) which is known as Rayleigh scattering but if the light is scattered inelastically, scattered lights can be specified Stokes and Anti-Stokes. When the scattered light frequencies smaller than (v_0), it is known as Stokes component of the spectrum and standed for $(v_0 - v_{ib})$, while the frequency of the scattered light greater than (v_0), it is called Anti-Stokes components and standed for $(v_0 + v_{ib})$ (Anderson and Dekker, 1971). As a consequence of the Boltzmann energy distribution, electrons are most probably to be in their lowest energy state at normal temperatures so stokes scattering is much more prevalent than anti-Stokes. For this reason, a spectrum of Stokes scattering is much more intense than a spectrum of anti-Stokes scattering; hence only Stokes scattering is generally used in Raman spectroscopy.

3.5.2.2 Experimental set-up for raman

The Raman measurements were conducted at room temperature by utilizing Bruker Optics FT-Raman Scope III system. The Raman spectra was excited by a 532 nm line of laser diode focused on the sample surface by a 100X Olympus microscope objective in the backscattering geometry. The laser power was kept at 20 mW. The scattering light was collected by a cooled CCD detector with 50 μm aperture. Spectral resolution was 0.5 cm^{-1}.

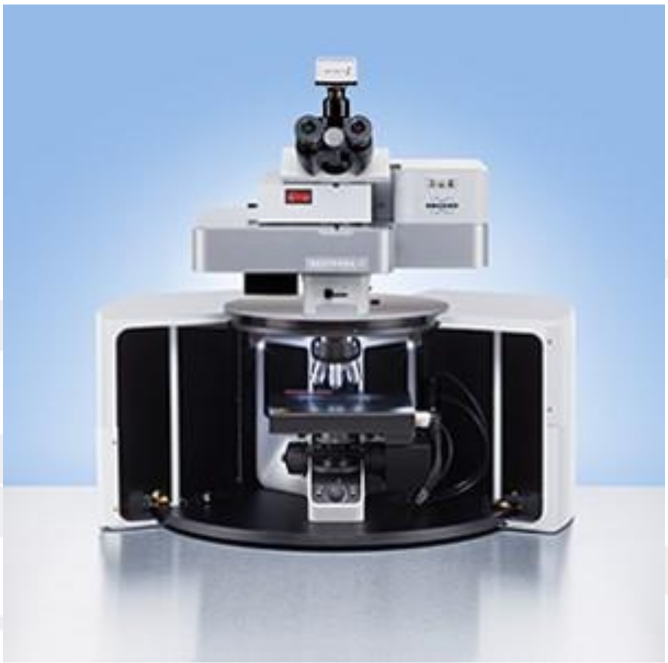

Figure 3.18: Experimental set-up for Raman Spectroscopy.

CHAPTER 4

4. RESULT AND DISCUSSION

4.1 Introduction

The purpose of this chapter is to demonstrate the experimental results of bulk $GaAs_{1-x}Bi_x$ (0.012 <x <0.039) and $GaAs_{1-x}Bi_x$/GaAs Quantum Well (QW) with various Bi contents (Bi%=1%, 2%, 3%) samples, grown on (100) and (311) B GaAs substrates acquired during the research. The structural characterization of these samples investigated by using XRD and AFM while the optical characterization of these samples investigated by PL and Raman spectroscopy is presented and discussed below. In section 4.2, the XRD properties of bulk $GaAs_{1-x}Bi_x$ and $GaAs_{1-x}Bi_x$/GaAs QW samples with various Bi contents (Bi%=1%, 2%, 3%), grown on (100) and (311) B substrates are presented. The study of the AFM in these samples is demonstrated in section 4.3. In section 4.4, the photoluminescence characteristics of the samples are presented. As a consequence, Raman spectroscopy results are given in section 4.5.

The information on the samples studied in the scope of this work on thesis is given in Table 4.1 and the structures of the samples are given in Figures 4.1 and 4.2. The bulk GaAs sample is shown in Figure 4.1 as a control sample and GaAsBi sample while GaAsBi QW sample is presented in Figure 4.2. Bulk samples are semiconductors grown on different orientations with a thickness of 1 µm on GaAs substrates at different temperatures and different Bismuth concentrations (Bi: 0.012 <x <0.039). The studied structures were grown by MBE on SI GaAs (100) and (311) B oriented substrates. The thickness of the enlarged $GaAs_{1-x}Bi_x$ layer was ~1 µm in all samples. The control samples of these samples was grown on (311) GaAs substrate two different temperatures of 350 °C and 580 °C. Thus, the contribution of Bi atoms to the structure can be understood by control samples.

In the light of results and experiences in bulk samples: $GaAs_{1-x}Bi_x$/GaAs single quantum well semiconductor systems are grown at high quality. (Structural and optical characterization experiments have shown to grow at high quality). For the improvement of the present samples are: $GaAs_{1-x}Bi_x$/GaAs single-quantum well semiconductors that were grown on by MBE on SI GaAs (100) and (311) B oriented substrates. The growth of GaAsBi QW samples started a 300 nm thick GaAs buffer layer at 580°C then the growth temperature was declined to 350°C to improve the incorporation of Bi in the QW. Then a 10 nm thick GaAsBi QW layer was grown followed by a 50 nm GaAs cap layer grown at the same temperature (see Figure 4.2). The growth rate was 0.45 µm/h for all layers. For efficient Bi incorporation, the atomic Ga/As flux ratio for the QW and cap layers was close to the stoichiometric value and the Bi concentration varied from 1% to 3%.

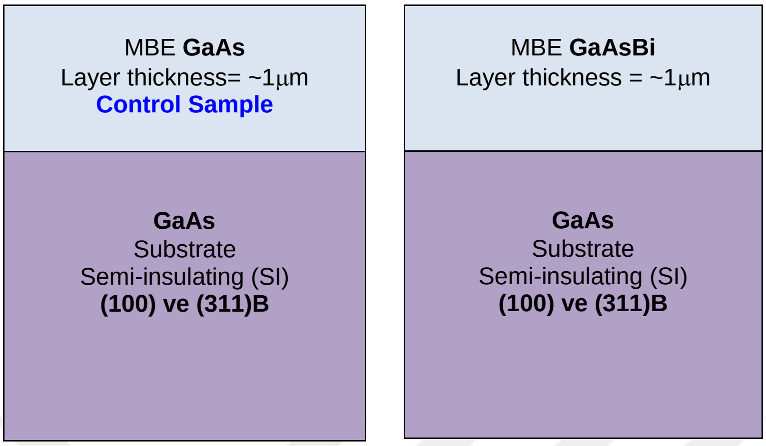

Figure 4.1: Bulk GaAs and GaAsBi structures.

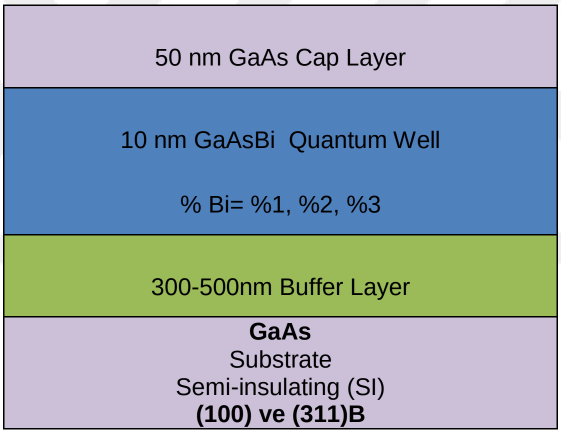

Figure 4.2: Layer structure of $GaAs_{1-x}Bi_x$/GaAs single-quantum well semiconductors.

Bulk $GaAs_{1-x}Bi_x$ and $GaAs_{1-x}Bi_x$/GaAs single-quantum well samples supplied from University of Nottingham were grown in a Veeco Modular Gen II MBE reactor equipped with a real-time wafer temperature sensor, which allows accurate monitoring of the substrate temperature during growth. The thickness of the $GaAs_{1-x}Bi_x$/GaAs single-quantum well layer as determined from growth parameters and verified by backscattering spectrometry was nearly 10 nm. The Bi concentration ranged from 1% to 3%. A nominally bulk GaAs and GaAsBi structures were used as a standard for comparison; GaAs and GaAsBi layers were a ~1μm–thick.

Table 4.1: List of samples investigated in this work with bismuth concentration.

Sample Name	**Growth Direction**	**Definition**	**Bi Concentration (%)**
Ms819	(100)	GaAsBi (Growth temperature 350^{o}C) (Annealing temperature 200 ^{o}C 3 hours)	0.012-0.039
Ms823	(311)B	GaAsBi (Growth temperature 350^{o}C) (Annealing temperature 300 ^{o}C 2 hours)	0.012-0.039
Ms824	(311)B	GaAsBi (Growth temperature 350^{o}C)	0.012-0.039
Ms827	(311)B	GaAs (Growth temperature 350^{o}C)-Control sample	0.012-0.039
Ms829	(311)B	GaAs (Growth temperature 580^{o}C)-Control sample	0.012-0.039
4144c	(100)	GaAsBi Quantum Well (Growth temperature 350^{o}C)	1.0
4145c	(100)	GaAsBi Quantum Well (Growth temperature 350^{o}C)	2.0
4153c	(100)	GaAsBi Quantum Well (Growth temperature 350^{o}C)	3.0
4151	(311)B	GaAsBi Quantum Well (Growth temperature 350^{o}C)	1.0
4152	(311)B	GaAsBi Quantum Well (Growth temperature 350^{o}C)	2.0
4154	(311)B	GaAsBi Quantum Well (Growth temperature 350^{o}C)	3.0

4.2 X-ray Diffraction (XRD) Results

The structural properties of the samples were determined by X-ray diffraction. XRD results for the bulk and quantum well $GaAs_{1-x}Bi_x$/GaAs samples are given in Figure 4.3.

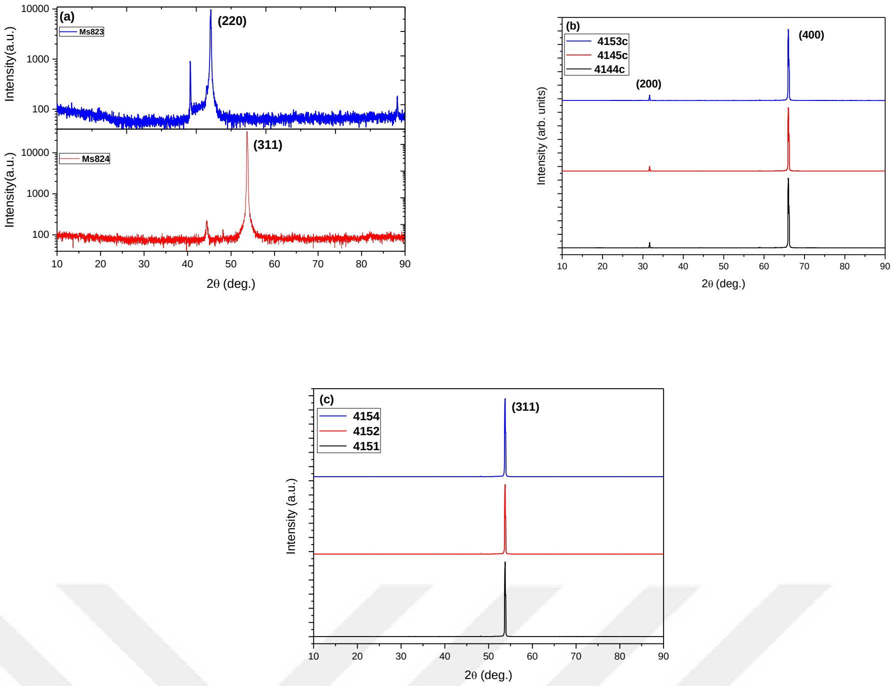

Figure 4.3: XRD spectra of **(a)** Bulk GaAs$_{1-x}$Bi$_x$, **(b)** (100) and **(c)** (311) B Quantum well GaAs$_{1-x}$Bi$_x$ /GaAs structures

The XRD spectrum taken in the bulk structure (a) shows that the crystal quality is not very high. In the graphs of Figures 4.3 (b) and (c), a very high quality result was obtained when the structure was grown in the form of a quantum well. These results were supported by AFM measurements. The surface roughness values were reduced to nm or even pm regardless of the magnification direction in the well structures, while in bulk structures greater than 20 nm. The positive developments in both optical and structural properties of well structures have been proven experimentally.

4.2.1 High Resolution X-ray Diffraction (HRXRD) Results

Double crystal X-ray rocking curve measurements were carried out by Panalytical X'Pert Pro MRD HRXRD system. All measurements were performed around GaAs (004) symmetry axis for GaAs$_{1-x}$Bi$_x$ SQWs grown on (100) substrates and GaAs (113) symmetry axis for GaAs$_{1-x}$Bi$_x$ SQWs grown on (311)B substrates by using Cu K$_{\alpha1}$ radiation (λ = 0.15406 nm).

The samples were characterized with high-resolution X-ray diffraction (HRXRD) measurements. (004) and (113) GaAs symmetrical reflections were recorded for the GaAs$_{1-x}$Bi$_x$ (x= 1%, 2%, and 3%) single quantum wells grown on (100) and (311) substrates, respectively. Figure 4.4 (a) and (b) show selected HRXRD curves (ω/2θ scans) measured at an X-ray wavelength of λ=1.5406 A^0 (Cu K$_\alpha$1) from six GaBiAs epilayers grown under near-stoichiometric conditions on (100) and on (311) B GaAs substrates .In order to determine the Bi content and QW thickness with HRXRD measurements.

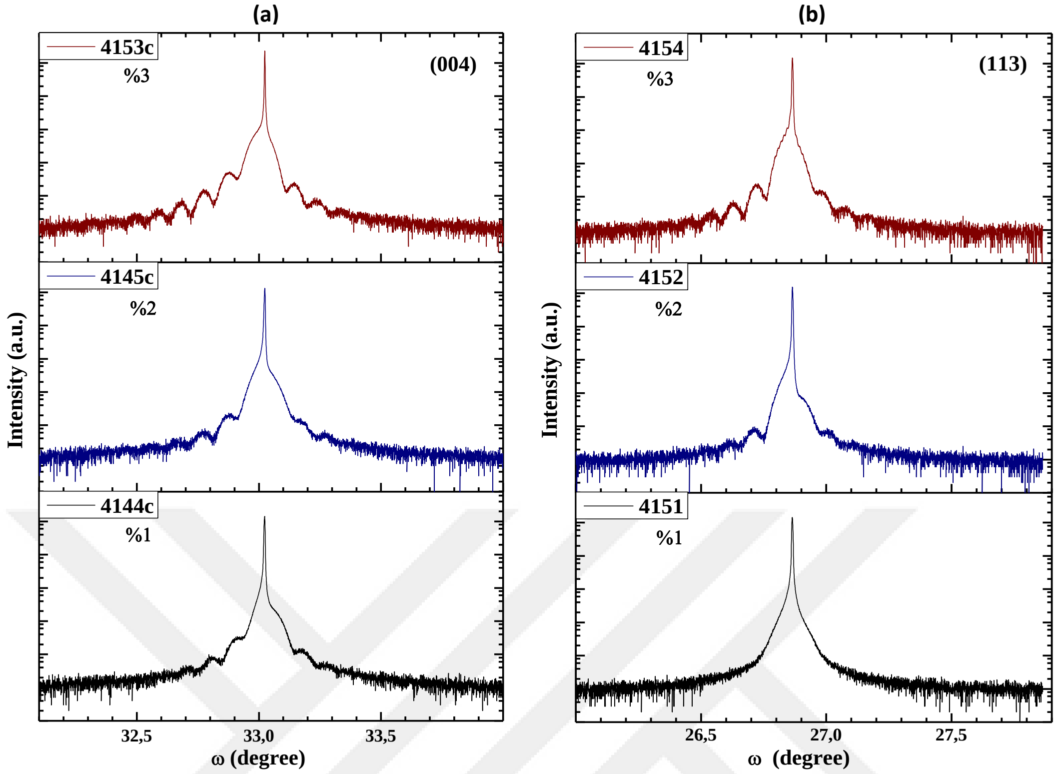

Figure 4.4: Symmetric rocking curves of $GaAs_{1-x}Bi_x$ SQWs.

A narrow peak and clear pendellosung fringes were observed for all samples except for the $GaAs_{1-x}Bi_x$ SQWs x=1% Bi concentration with grown on (311) B GaAs substrate. By the 4151 sample the pendellosung fringes have completely disappered, indicating that the uniformity of the capping layer lattice constant has become sufficiently distorted to annihilate constructive interference between the x-ray scattered from the sample and the top QW interface. Since the fringes are sensitive to the crystalline quality and interface quality, the disappearance of the fringes for the sample grown mainly caused by the structure defects and interface destruction (Fitouri et al, 2008; Moussa I et al, 2008). The presence of more peaks in the XRD patterns may be ascribed to a phase separation in the GaAsBi alloy (Oe, 2002) or the presence of micro-regions with different Bi content (El-Masry, 1998).

According to the XRD spectra, in the series of samples of increasing Bi% concentration grown on (100) and (311) B crystalline planes 2θ were observed as (33) and (26.9) degrees and denoted as 4144c, 4145c and 4153c grown on (100) planes and 4151, 4152 and 4154 grown on (311) B planes samples codes, respectively. The XRD pattern of the GaAsBi alloy shows that the structure is crystallized in the cubic phase. The XRD pattern of examination displayed that there are different orientations and different %Bi concentrations of the GaAs semiconductors.

The geometry of peaks is related fundamentally to the positions of the atoms within the crystallite unit cell, with little regard to the nature of these atoms. The peaks and grain sizes can be seen for each sample in Table 4.2. Compare with the (100) planes, there are a small peaks appearing at lower reflection angles for the (311) B planes. The XRD peaks of GaAsBi SQWs are seen to be broader in (311) B oriented than in (100) oriented. Intensity of peaks are increased with the increasing Bi% concentration grown on (100) GaAs substrate. Intensity of peaks which are located (311) B of much lower value than the (100) orientations. In addition, the full-width at half maximum (FWHM) of the XRD peaks for both orientations are calculated. The FWHM of XRD peaks are calculated as 0.00448, 0.00434 and 0.00281 nm and observed decreasing with the increasing Bi% concentration grown on (100) planes which do not have any bismide metallic segregation on the surface. The FWHM of XRD peaks for the samples (311) B plane are calculated as 0.00448, 0.00388 and 0.00397 nm. Compared with the others samples grown on (311) B plane, the full-width at half maximum (FWHM) of the XRD peak is higher for 1% Bi concentration of single quantum well. In fact, the FWHM of (311) B oriented GaAsBi alloy were found to increase with rising Bi concentrations. This suggests the quality of the (311) B GaAsBi SQWs are poor and having a substational degree of structural disorder. The intensity and width of the substrate reflections are compared for both orientations, a much smaller relative intensity is observed from the (311) B GaAsBi SQWs. This indicates considerably thinner epilayer in the (311) B direction.

The average grain size (D) in the (hkl) plane direction was calculated from the full-width at half maximum (FWHM) of the XRD peaks by using the Scherrer formula:

$$D = \frac{K\lambda}{\beta cos\theta} \tag{22}$$

where K is a dimensionless shape factor (~0.94), λ (1.5406 Å) is the X-ray wavelength, β is the observed angular width at half maximum intensity (FWHM) of the peak and θ is the Bragg angle (Cullity,1958).

For a crystal lattice in a cubic structure, the unit cell parameters (a = b = c) and the d-spacing between atomic planes are characterized by the following equation (Cullity, 1966)

$$\frac{1}{d_{hkl}^2} = \frac{h^2+k^2+l^2}{a^2} \tag{23}$$

Also, Bragg's law which is defined as $2d\ \sin\theta = n\lambda$ is used for the calculations of XRD parameters. It is concluded that the grain size and FWHM were increased in the samples that have surface segregation.

Table 4.2: The measured and calculated X-ray diffraction parameters for $GaAs_{1-x}Bi_x$ SQW.

Sample	Observed Data		Standart Data		*FWHM* (deg.)	Grain Size (*Å*)	Cell Parametres *a=b=c* (*Å*)		(*hkl*)
	2θ (deg.)	*d* (*Å*)	2θ (deg.)	*d* (*Å*)			Calculated	Standard	
4153c (3% Bi)	31.672	2.822	31.65	2.825	0.100	857.97	5.6440	5.6538	(*200*)
	66.044	1.413	66.04	1.414	0.112	885.20	5.6520	5.6538	(*400*)
4145c (2% Bi)	31.672	2.822	31.65	2.825	0.095	904.16	5.6440	5.6538	(*200*)
	66.005	1.413	66.07	1.414	0.145	682.54	5.6563	5.6538	(*400*)
4144c (1% Bi)	31.680	2.822	31.65	2.825	0.093	924.85	5.6440	5.6538	(*200*)
	66.056	1.413	66.04	1.414	0.102	967.07	5.6774	5.6538	(*400*)

Sample	Observed Data		Standart Data		*FWHM* (deg.)	Grain Size (*Å*)	Cell Parametres *a=b=c* (*Å*)		(*hkl*)
	2θ (deg.)	*d* (*Å*)	2θ (deg.)	*d* (*Å*)			Calculated	Standard	
4154 (3% Bi)	53.782	1.703	53.750	1.704	0.117	791.80	5.7227	5.6520	(*311*)
4152 (2% Bi)	53.783	1.703	53.750	1.704	0.102	915.89	5.6459	5.6520	(*311*)
4151 (1% Bi)	53.787	1.703	53.750	1.704	0.097	951.84	5.6476	5.6520	(*311*)

As shown in Figure 4.4, the fringes around the main GaAs peak were observed for all samples except for the one (4151). These interference fringes arise from the phase shift between GaAs cap and buffer layers (i.e. the fringe spacing gives a way of measuring the thickness of GaAs cap layer). The GaAs cap layer thicknesses were determined from x-ray rocking measurements and are shown in Table 4.3 for all samples. For sample 4151, the lack of fringes can be attributed to the roughness of the epilayer surface or unsmooth interfaces and compositional inhomogeneity.

Table 4.3: The thickness of GaAs cap layers calculated from X-ray rocking curve measurements for $GaAs_{1-x}Bi_x$ SQWs

Sample ID	**4144c**	**4145c**	**4153c**	**4151**	**4152**	**4154**
The thickness (nm)	55.8	54.6	55.8	-	52	55

Vegard's law has been used to estimate the concentration of the semiconductors alloys (Vegard, 1921). Finding out the lattice parameters by XRD measurements, the concentration of the ternary alloys can be calculated from equation (24) representing Vegard's law. The lattice constant of zincblende GaBi is unknown experimentally therefore the approximate concentration values can be obtained by using a hypothetical lattice constant of zincblende GaBi (a(GaBi)=6.33 Å) (Tixier, 2003). When examining X-ray rocking curves, it has been expected a broad peak representing $GaAs_{1-x}Bi_x$ layer. In other words, the broad peak of $GaAs_{0.99}Bi_{0.01}$ layer should be appeared at around -1000 relative seconds (Tixier, 2003). However, it is not clearly seen in X-ray rocking curves due to very thin $GaAs_{1-x}Bi_x$ layers.

$$a(GaAs_{1-x}Bi_x)=(1-x)a_{GaAs} + x.a_{GaBi} \tag{24}$$

4.3 Atomic Force Microscopy (AFM) Results

Structural properties were determined by Park System AFM. The surface morphology is monitored by AFM. Because of the large difference between the atomic volume of Bi (21.3 cm^3/g atom) and As (13.1 cm^3/g atom), incorporating Bi with GaAs during the low temperature growth lead to extended defects (Rodrigoa et al., 2010).

AFM results of bulk $GaAs_{1-x}Bi_x$ and $GaAs_{1-x}Bi_x$ SQWs which were grown on (100) and (311) B shown in Figure 4.5, 4.6 and 4.7, respectively. There isn't any Bi droplet or segregation is observed in $GaAs_{1-x}Bi_x$ SQWs.

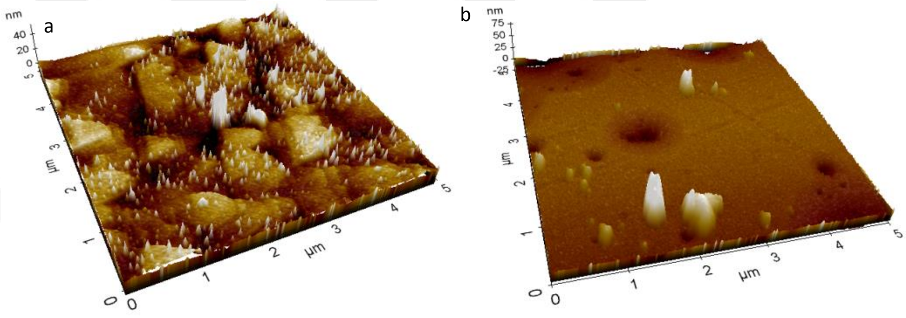

Figure 4.5: AFM images of **(a)** Ms823 and **(b)** Ms824 bulk $GaAs_{1-x}Bi_x$/GaAs structures.

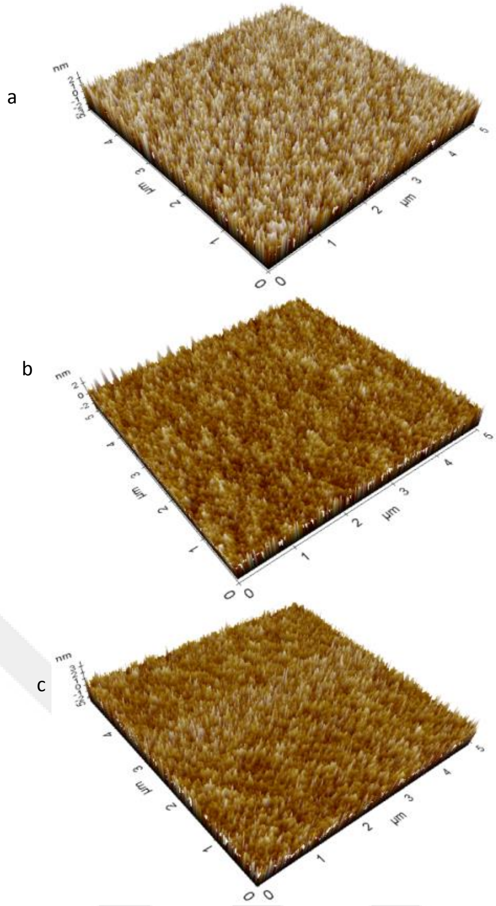

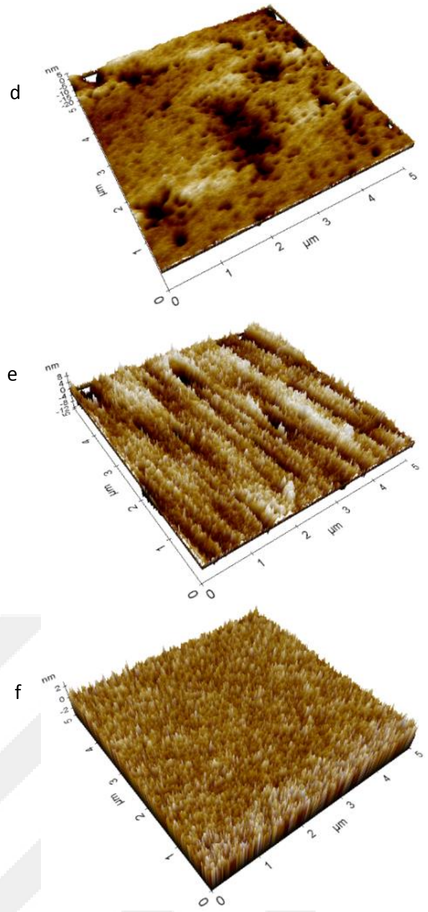

Figure 4.6: AFM images of $GaAs_{1-x}Bi_x/GaAs$ SQW **(a)** 4144c (1%Bi), **(b)** 4145c (2%Bi) and **(c)** 4153c (3%Bi)

Figure 4.7: AFM images of $GaAs_{1-x}Bi_x/GaAs$ SQW **(d)** 4151 (1%Bi), **(e)** 4152 (2%Bi) and **(f)** 4154 (3%Bi)

4.4 Photoluminescence (PL) Results

The photoluminescence measurements performed to determine the optical transition energies of quantum well systems which were grown on (100) and (311) B orientations at different concentrations (Bi%=1%, 2%, 3%) within the scope of the thesis have been completed depending on the temperature and power. Figure 4.8 and Figure 4.9 shows the shift in band energy due to both temperature and power, respectively. The photoluminescence results of the bulk structures are not presented in the thesis because they contain very high noise.

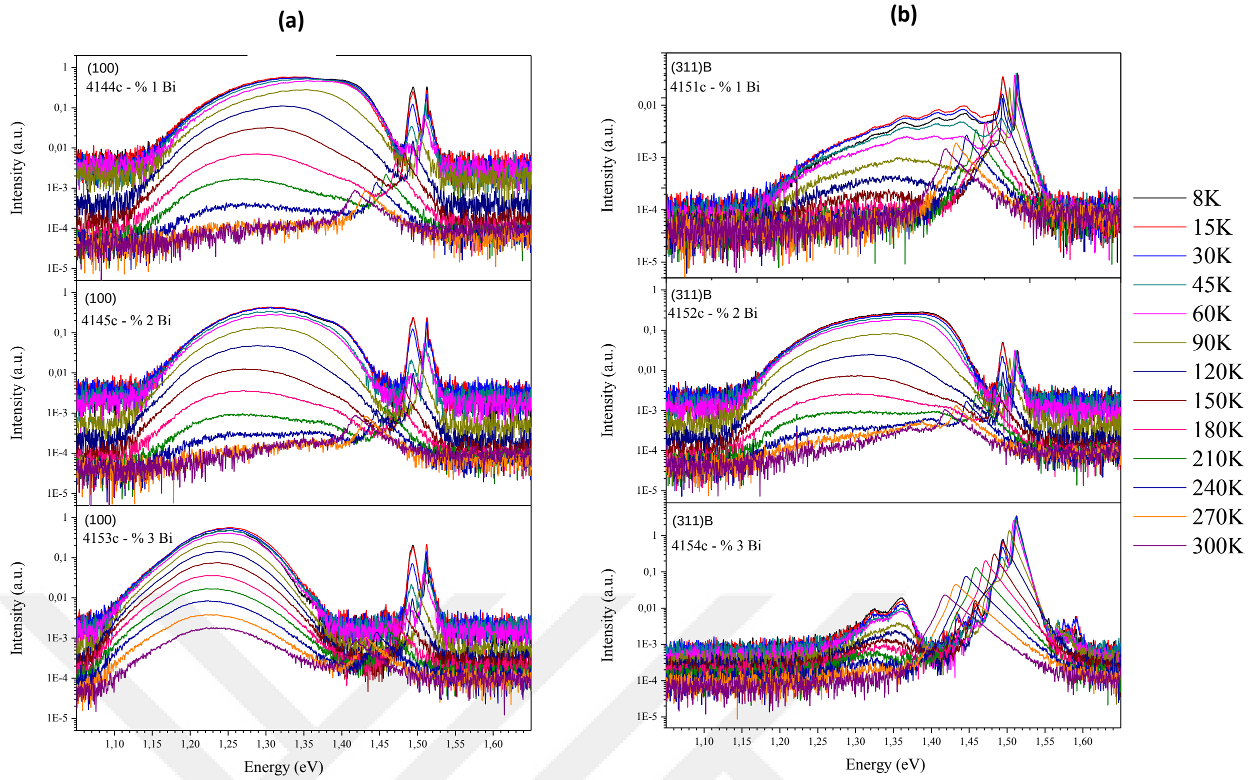

Figure 4.8: PL spectra of GaAsBi QW structures at temperatures between 8 K and 300 K growth on (a) (100) and (b) (311) direction.

In Figure 4.8, it is clearly shown that the incorporation of Bi atoms into III–V host modifies both the conduction band (CB) and the valence band (VB). The observation can be explained band gap reduction as a result of introduction of the Bi into the structure increasing number of Bi-related non-radiative centers. The band gap reduction of the $GaAs_{1-x}Bi_x$ alloys approximately 40 meV/% Bi. However, on bulk GaBiAs samples, the shrinkage of the band gap was reported 90 meV/%Bi up to 3 % concentration (Sarcan et al., 2014). Bi-induced reduction of the band gap in $GaAs_{1-x}Bi_x$ is assigned to the interaction between Bi-induced levels with the valence band (VB) states of GaAs host. According to VBAC model this reduction should appear in the VB but recent tight-binding calculations (Usman et al., 2011) suggest that the incorporation of Bi atoms into GaAs host modifies both the conduction band (CB) and the valence band (VB). This conclusion has also been confirmed by photoreflectance studies of the band structure of $GaAs_{1-x}Bi_x$/GaAs quantum wells (QWs) as well as by the density functional theory (DFT) calculations of the band structure of $GaAs_{1-x}Bi_x$ alloys. These results clearly show that the narrowing of the band gap in this alloy is due to both the VB upward shift and the CB downward shift (Kudrawiec et al., 2014). Very similar conclusions have been obtained within the DFT calculations of $GaSb_{1-x}Bi_x$ (Samajdar and Dhar, 2015). The chemical trends of the band gap reduction are very apparent: the bigger the difference in terms of atom size, lattice constant and electronegativity between the parent III–V compound and its bismuth containing counterpart, the more pronounced the effects.

Figure 4.9 shows photoluminescence results taken at power values of 0.083mW-51mW. As the excitation power, Pex was increased from 0.083 to 51 mW, the PL peak become blue-shifted (~35 meV) and this effect is explained by the localization effect. The localization effect in GaAsBi structures is usually originated from alloy disorder. In addition, Bismuth clusters in the structure and interfacial disturbances in the region between the quantum well and the barrier are a consequence of the localization effect. When the excitation power is increased, carriers can be excited to higher energy levels in the well and it can be observed the energy is blue shifted.

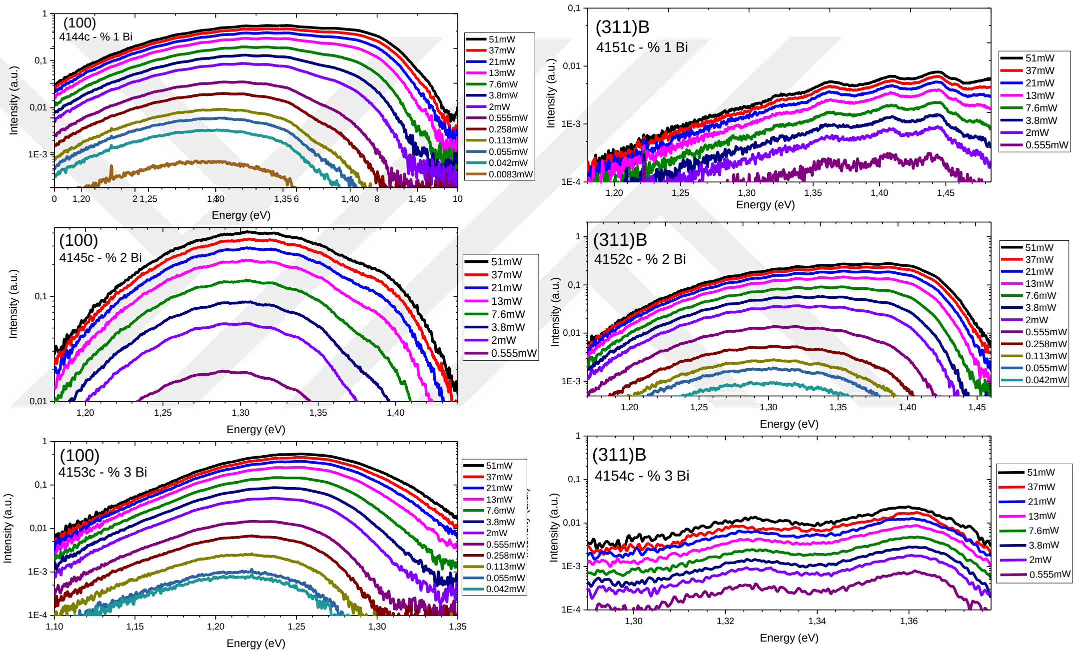

Figure 4.9: PL spectra of GaAsBi QW structures at power values of 0.083mW-51mW growth on (a) (100) and (b) (311) direction.

As a consequence of the Bi related defect levels, the S-shape behavior, that is, in the presence of defects the emission occurs due to localized excitions at low temperatures. The redistribution of excitons over deep localized states brings the red shift. However, at intermediate temperature the carriers gain sufficient thermal energy which induces delocalization of the carriers so emission is pronounced to the delocalized carriers in the structure (Kopaczek et al., 2015). In other words, the escape of excitons to delocalized states give rise to the blue shift.

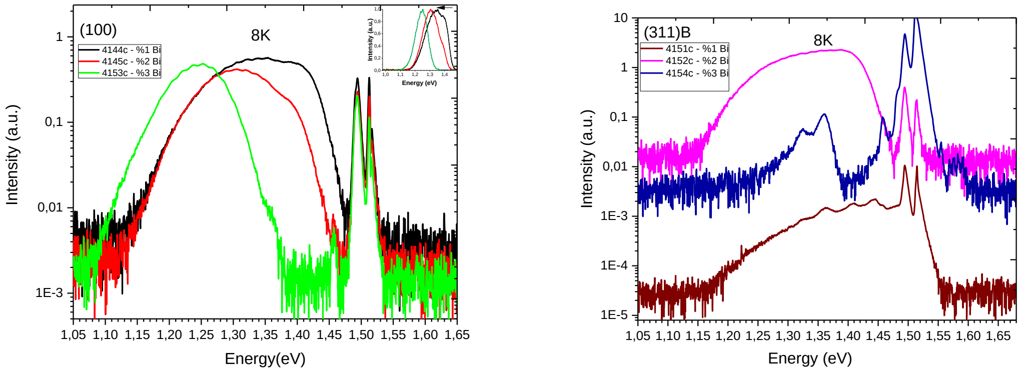

Figure 4.10: Photoluminescence spectra of quantum well samples at 8 K

Figure 4.10 shows the graph of the normalized photoluminescence peak energies at 8 K. The band gap decreases with increasing Bi concentration for both structures grown on (100) and (311) B orientations. However, the decrease in band gap energies is different in growth directions. The band gap energy value for the structure growth on (100) and (311) B changes from 1,34 eV to 1,24 eV and 1,43 eV to 1,35 eV, respectively (that is shown in Table 4.4) Incrementation Bi composition results in the band gap reduction in both samples growth on (100) and (311) B due to not only band anti-crossing (BAC) interaction in the valence band (VB) but also conventional alloy behavior in the conduction band (CB) (Usman et al., 2011). Also, it is clearly visible that the emission peak demonstrates a blue shift with the increase of Bi concentration in the samples growth on (100) orientation. It is apparently seen that there is additional energy levels which result from the effect of Bi pair and cluster states in GaAsBi structure.

Table 4.4: Photoluminescence peak energies at 8 K. It shows that the decrease in the band energy due to the Bi concentration decreases independently of the direction.

Samples	**Photoluminescence Energy (eV)**
4144c (%1 Bi, 100)	1.34
4145c (%2 Bi, 100)	1.30
4153c (%3 Bi, 100)	1.24
4151 (%1 Bi, 311)	1.43
4152 (%2 Bi, 311)	1.34
4154 (%3 Bi, 311)	1.28

4.5 Raman Spectroscopy Results

Raman measurements performed on $GaAs_{1-x}Bi_x$ (x = 1%, 2% and 3%) QW structures grown on (100) and (311) B GaAs substrates in order to investigate the lattice vibration properties of the structures have been presented in Figure 4.11 and Figure 4.12. Arrows represent GaAs crystal phonon modes in normalized Raman spectra. As indicated in the literature before, GaAs TO and LO phonon modes appear at ~ 267 and 290 cm^{-1}, respectively (Verma et al., 2001). In a zincblende crystal (T_d site symmetry), the GaAs LO(Γ) phonon is permitted, but, the GaAs TO(Γ) is forbidden in respect to Raman selection rules in these scattering geometries. As seen in Figure 4.12, there is a dominant presence of TO(Γ) in Raman Spectrum can be assigned bizmuth-induced disorder in the lattice. The observed peaks at ~ 185 and 213 cm^{-1} are transverse optical (TO) and longitudinal optical (LO) phonon modes for GaAs namely, GaBi TO (Γ) and LO (Γ) phonon modes. LO(Γ) phonon mode shifts toward lower frequencies and there is a systematic decline in Raman intensities by increasing Bi concentration in the samples which were grown on (100) and (311) B orientations. This result is due to the fact that the increase in the amount of Bi atoms incorporated into the structure causes a decrease in crystal quality. In comparison to reference GaAs sample, GaAsBi samples exhibit a broad band in spectral range at around 180−230 cm^{-1} that is indicated a disorder-activated TO (DATO) mode (Steele et al., 2013).

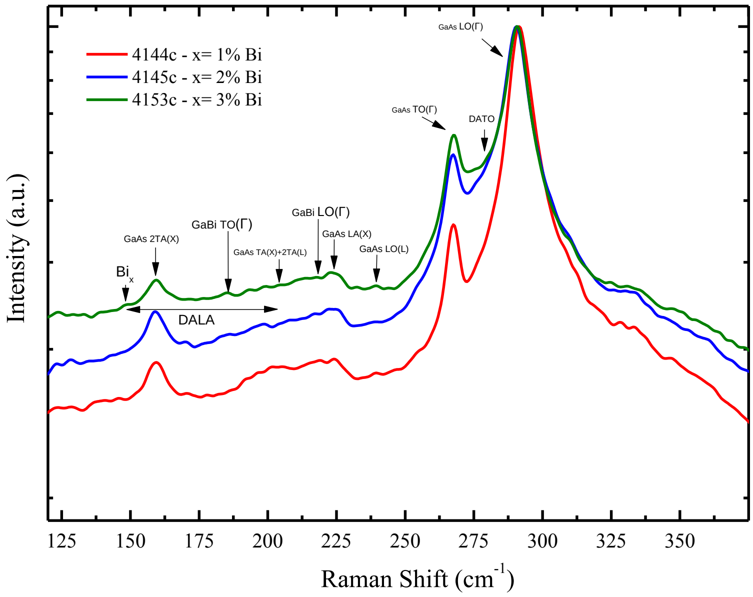

Figure 4.11: Raman spectra of $GaAs_{1-x}Bi_x$ grown on (100) (x = 1%, 2% and 3%)

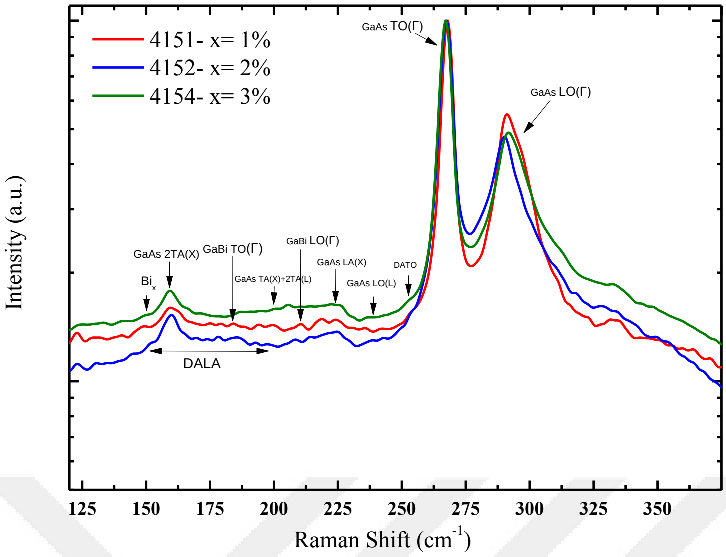

Figure 4.12: Raman spectra of GaAs$_{1-x}$Bi$_x$ grown on (311) B (x = 1%, 2% and 3%)

As shown in Figure 4.12, a weak broad feature appears at ~ 200 cm^{-1} for GaAs$_{0.99}$Bi$_{0.01}$. It represents GaAs TA(X)+2TA(L) phonon modes which is attributed to higher-scattering combination (Steele et al., 2013). Besides, with increasing Bi concentration, the weak features are appeared at ~ 223 and 239 cm^{-1} which are attributed to GaAs LA(X) and LO(L) phonon modes, respectively. The observed LA(X) and LO(L) phonon modes should be related to Bi resonant levels which result in GaAs valence bands mixing due to Bi incorporation (Seong et al., 2005). It is clearly seen in Figure 4.13 that GaBi TO(Γ) phonon mode becomes clear for GaAs$_{0.98}$Bi$_{0.02}$ and becomes more visible with increasing Bi concentration. On the other hand, GaBi LO(Γ) phonon mode could not be distinguished clearly. It should be related to dominant TA(X)+2TA(L) phonon modes. For GaAs$_{0.97}$Bi$_{0.03}$, a weak feature at ~140 cm^{-1}, labeled Bi$_x$, is of unclear origin may also be attributed to Bi content (Verma, 2001).

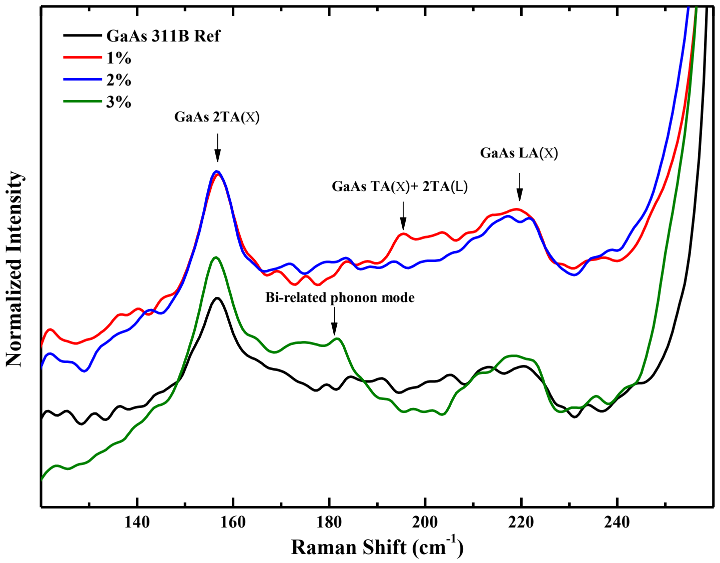

Figure 4.13: Normalized Raman spectra of $GaAs_{1-x}Bi_x$ grown on (311) B (x = 1%, 2% and 3%)

As can be seen in Figure 4.13, a closer look to normalized Raman spectra within a range of 120-260 cm^{-1} reveals that the Bi-related phonon mode at ~181 cm^{-1} is more prominent for $GaAs_{0.97}Bi_{0.03}$. For $GaAs_{0.97}Bi_{0.03}$, the feature at ~214 cm^{-1} is determined as resulting from substitutional Bi at the As site (BiAs) in GaAsBi due to Bi-induced lattice deformation and this phonon mode is nominated the new GaBi phonon mode in the literature (Seong et al., 2005).

Difference in atomic radius and electronegativity between Arsenic (As) and Bismuth (Bi) is smaller than many ternary semiconductor alloys so it is expected that much smaller Bi-induced lattice deformation in $GaAs_{1-x}Bi_x$ (Seong et al., 2005). Also, As content is very high compared to the Bi content so it is anticipated that GaBi-like mode should be weaker than GaAs-like mode. Increment of Bi content causes increase in the intensity of the first-order phonon, whereas the intensity of second order phonons present a small decline with increment of Bi content. Increase in Bi content give rise to second-order phonons intensity decrease in samples which can be described by relaxation in the momentum selection rules. It make sense that the strong Raman scattering intensities of the GaAs-like modes compared to GaBi-like modes as the Bi contents in these samples are much smaller than the As contents (Verma, 2001).

The features at between 210-250 cm^{-1} show the broad structure for the GaAsBi structures which is similar to previously observed (Lannin, 1977) and vibrational modes indicating to As clusters in GaAs. Due to the low growth temperature, incorporation of Bi atoms into the lattice structure lead to form As clusters in the samples, which can be clearly seen in Raman spectra. However, incorporation of Bi increase incline to increment of the amount of knocked-out As atoms, and thus the strength of this structure has a weak dependence on the Bi content of samples (Verma, 2001).

Table 4.5 shows the optical phonon energies that occur in the resulting structure of the lattice vibrations with the GaBi LO mode obtained from the Raman measurements. A systematic optical phonon energy calculation in this way has not been reported in the literature on working GaAsBi materials systems.

Table 4.5: Optical phonon energies of Bi-containing structures.

	GaBi LO(Γ) (cm^{-1})	**Energy (meV)**
4144c (100) %1 Bi	219,02	27,16
4151 (311)B %1 Bi	210,43	26,10
4145c (100) %2 Bi	217,05	26,92
4152 (311)B %2 Bi	208,25	25,83
4153c (100) %3 Bi	217,60	26,99
4154 (311)B %3 Bi	210,46	26,10

As shown in Table 4.5, the optical phonon energy depends on growth direction. The optical phonon energy decreases with increasing of the growth orientation.

CHAPTER 5

5. CONCLUSIONS

The principal of the current thesis was to investigate the effect of dilute bismuth composition and growth orientation on material properties such as structural, optic and electrical properties. In this research thesis, different features have been found and studied for different Bi containing compounds and growth orientations. MBE grown Bismuth containing compounds bulk $GaAs_{1-x}Bi_x$ ($0.012 < x < 0.039$) and $GaAs_{1-x}Bi_x$/GaAs Quantum Well (QW) with various Bi contents (Bi%=1%, 2%, 3%) samples are investigated by X-ray diffraction (XRD), Atomic Force Microscopy (AFM), Photoluminescence (PL) and Raman Spectroscopy and then crystal structure, surface morphologies, structural and optical properties are explored from these characterizations, respectively.

The structural properties of the samples were determined by X-ray diffraction (XRD). As it is understood from the XRD spectrum, the bulk structure shows that the crystal quality is not very high while for the quantum well structures shows a very high quality results. High resolution X-ray diffraction results show that the structure is crystallized in the cubic phase. The XRD peaks of GaAsBi SQWs are seen to be broader in (311) B oriented than in (100) oriented. Intensity of peaks are increased with the increasing Bi% concentration grown on (100) GaAs substrate. Intensity of peaks which are located (311) B of much lower value than the (100) orientations. In addition, the full-width at half maximum (FWHM) of the XRD peaks is decreasing with the increasing Bi% concentration grown on (100) plane while it is increasing with Bi% concentration grown on (311) B plane. This presents the quality of the (311) B GaAsBi SQWs are poor and having a substational degree of structural disorder. In conclusion, the observation of the fringes indicates that the grown structures have high crystalline quality and the x-ray diffraction simulations reveal that $GaAs_{1-x}Bi_x$ SQWs were grown properly. These results were supported by AFM. The surface morphology is monitored by AFM and there isn’t any Bi droplet or segregation is observed in $GaAs_{1-x}Bi_x$ SQWs.

The photoluminescence measurements performed to determine the optical transition energies of quantum well systems which were grown on (100) and (311) B orientations at different concentrations (Bi%=1%, 2%, 3%) within the scope of the thesis have been completed depending on the temperature and power. The photoluminescence results of the bulk structures are not presented in the thesis because they contain very high noise. Introduction of the Bi into the structure increasing number of Bi-related non-radiative centers so band gap reduction is observed. As the temperature and excitation power were increased, the PL peak become blue-shifted. Bi-related defects in crystalline structure by growing the high-index plane and decreasing the non-radiative transitions in the structure which is a contribution to optical quality enhancement was investigated within the scope of the thesis. It is thought that the presence of bismuth (Bi) modifies both conduction and valance band of the host semiconductor. The bismuth incorporation into the structure which causes the defects in the structure has been given literatures with structural and morphological studies.

Raman measurements based on $GaAs_{1-x}Bi_x$ (x = 1%, 2% and 3%) QW structures grown on (100) and (311) B GaAs substrates in order to investigate the lattice vibration properties of the structures. Arrows represent GaAs crystal phonon modes in normalized Raman spectra. According to Raman spectroscopy results there is a dominant presence of TO(Γ) in Raman spectrum can be assigned bismuth-induced disorder in the lattice and LO(Γ) phonon mode shifts toward lower frequencies so there is a systematic decline in Raman intensities by increasing Bi concentration in the samples which were grown on (100) and (311) B orientations. Therefore, the increase in the amount of Bi atoms incorporated into the structure causes a decrease in crystal quality.

As a consequence, in the thesis, diluted bismuth materials have been investigated under the project for the effect of the growth temperature, to determine the defects in the structure and to reduce the effects of defects. For $GaAs_{1-x}Bi_x$/GaAs structures, it is not possible to use these structures in the construction of electronic devices without obtaining the growth parameters, defects, impurities, dislocations and perfect surface morphology. A limited number of experimental studies on the optical properties of the GaAsBi semiconductor system are available in the literature. The effects of different bismuth concentrations were investigated in the studies carried out, but a comprehensive research on the effect of different growth, annealing temperature and duration on the growth of high index has been presented for the first time with the thesis.

It has been proposed that the structures to be designed by determining the optimum growth conditions and doing characterization experiments and the structures will have the potential to be used in the laser production which emitted at wavelength of ~1.3 μm which is the operation wavelength for telecommunication window that is very important for fiber optic communication and this proposal has been confirmed with thesis outputs. As a result, the thesis has reached the targeted success in terms of innovations in the literature.

REFERENCES

Alberi K, Dubon O.D., Walukiewicz W., Yu K.M., Bertulis K., and Krotkus A. 2007. Valence band anticrossing in GaBixAs1-x, Applied Physics Letters, 91, 051909-051909-3.

Anderson A and Dekker M. 1971. The Raman Effect, INC, New York.

Anonymous. Research. Low Dimensional Quantum Systems. https://www.ucl.ac.uk/hirjibehedin/research/low-dimensional Access date: 27.06.2016

Anonymous. 2016. Quantum transport in low-dimensional systems. https://www.uclouvain.be/en-354422.html Access date: 27.06.2016

Arthur J R. 1968. J. Appl. Phys. 39, 4032.

Azadeh M. 2009. Fiber Optics Engineering. Optical Networks. Optical Fibers, pp 127-155.

Barron A R. 2016. Structures of Element and Compound Semiconductors. Group III-V (13-15) compounds. http://cnx.org/contents/wRnesIEI@6/Structures-of-Element-and-Comp Access date: 29.12.2016.

Baskaran S. 2010. Structure and Regulation of Yeast Glycogen Synthase.

Beaton D A. 2011. Electronic States and Transport in GaNxAs1-x and GaAs1-xBix.

Bertulis K, Krotkus A, Aleksejenko G, Pačebutas V, Adomavičius R, Molis G, Marcinkevičius S. 2006. APPLIED PHYSICS LETTERS 88, 201112.

Biasiol G and Sorba L. 2001. MOLECULAR BEAM EPITAXY: PRINCIPLES AND APPLICATIONS. Crystal growth of materials for energy production and energy-saving applications.

Blakemore J S. 1982. Semiconducting and other major properties of gallium arsenide. J. Appl. Phys. 53(10).

Bruesch P. 1987. Phonons: Theory and Experiments I, II and III, Springer Verlag, Berlin.

Bruce L. 1986. IEEE J. Quantum Electron. 22, 1909.

Chang L L, Ploog K. 1985. Molecular Beam Epitaxy and heterostructures, NATO ASI Series , Volume 87.

Cho A. 1971. J. Vac. Sci. Tech. 8, S31.

Cullity B D. 1958. Trans. Met. Soc. A.I.M.E., 212,764.

Cullity B D. 1966. Elements of X-Ray Diffraction. Adsison-Wesley Publishing Company, Inc., USA, 514p.

Device Research Laboratory. MBE Setups. Solid Source MBE. http://drl.ee.ucla.edu/?page_id=480 Access date: 30.12.2016

El-Masry N A,Piner E L,Liu S X,and Bedair S M 1998 Appl. Phys. Lett. 72 40

Erol A, Mazzucato S, Arikan M C, Carrere H, Arnoult A, Bedel E, Balkan N. 2003. Photo-induced transient spectroscopy of defect levels in GaInNAs. Semiconductor Science and Technology, 18, 968-972.

Fewster P F and Curling C J. 1987. Composition and latticemismatch measurement of thin semiconductor layers by x-ray diffraction. Journal of Applied Physics, vol. 62, p. 4154.

Fitouri H, Moussa I, Rebey A, Fouzri A, Jani B E. 2008. J. Cryst. Growth 295, 114.

Fluegel B, Francoeur S, Mascarenhas A, Tixier S, Young E C, and Tiedje T. 2006. Giant Spin-Orbit Bowing in GaAs1−xBix. Physical Review Letters, 97, 067205-067205-4.

Francoeur S, Seong M J, Mascarenhas A, Tixier S, Adamcyk M, Tiedje T. 2003. Band gap of GaAs1−xBix, 0<x<3.6%. Applied Physics Letters, 82, 3874-3876.

Geller M R. 2001. Quantum Phenomena in Low-Dimensional Systems. Fundamentals of Physics, Vol. II.

Grundmann M. 1999. Physica E 5, 167.

Gunes M., 2010. Optical and Electronic Properties of Nitrogen Containing III-V Compounds

Guina M. 2009. MBE growth of dilute nitrides, Training school. New Trends in III-V-N materials and devices lecture notes. Delphi.

Hayes W and Loudon R. 1978. Scattering of Light by Crystals, J.Wiley & Sons, New York.

Hilska J. 2016. Effect of growth parameters on the properties of GaAsBi.

Hsieh J J, Shan C C. 1977. Room-temperature CW operation of buried-stripe doubleheterostructure GaInAsP/InP diode lasers. Applied Physics Letters, 30, 429-431.

Hook J R and Hall H E. 1991. Solid State Physics. Second Edition. John Wiley & Sons.

Huang W, Oe K, Feng G, and Yoshimoto M.2005. Molecular-beam epitaxy and characteristics of GaNyAs1-x-yBix. Journal of Applied Physics, vol. 98, pp. 053505-6.

Ibach H. and Lüth. H. 2003. Solid-State Physics, An Introduction to Principles of Materials Science, forth ed. Springer Verlag.

Innovent Technologieentwicklung Jena Catalog. Crystal growth techniques. Liquid phase epitaxy. http://www.innovent-jena.de/en/INNOVENT-/Departments/Magnetic-and-optical-systems/Crystal-growth/Crystal-growth-technique__4853/#con-5642 Access date: 30.12.2016.

Joco V. 2008. Electronic structure of bulk and low dimensional systems analyzed by Angle-Resolved Photoemission Spectroscopy.

John in VLSI. 2011. Chemical Vapor Deposition (CVD). Epitaxial Reactors. http://www.circuitstoday.com/chemical-vapour-deposition-cvd Access date: 30.12.2016.

Kittel C. 2004. Introduction to Solid State Physics. Eight Edition, pp. 17.

Kondow M, Uomi K, Niwa A, Kitatani T, Watahiki S, Yazawa Y.1996. GaInNAs: a novel material for longwavelength-range laser diodes with excellent high-temperature performance. Japanese Journal of Applied Physics, 13, 1273-1275.

Kopaczek J, Linhart W M, Baranowski M, Richards R D, Bastiman F, David J P R and Kudrawiec R. 2015. Optical properties of GaAsBi/GaAs quantum wells: Photoreflectance, photoluminescence and time-resolved photoluminescence study. Semicond. Sci. Technol. 30 ,094005.

Kudrawiec R, Kopaczek J, Polak M P, Scharoch P, Gladysiewicz M, Misiewicz J, Richards R, Bastiman F, David J P R. 2014. Experimental and theoretical studies of band gap alignment in $GaAs_{1-x}Bi_x$/GaAs quantum wells. Journal of Applied Physics 116(23):233508.

Kuphal E. 1991. Liquid phase epitaxy. Applied Physics A 52(6):380-409.

Lannin J S.1977. Raman scattering properties of amorphous As and Sb. Phys. Rev. B 15, 3863.

Li S S. 1993. Semiconductor Physical Electronics. Plenum Press. New York and London.

Lopez N P, Tao J, Talbot J B, McKittrick J, Hirata G A and DenBaars S P. 2008. A novel hybrid pulsed laser deposition/metalorganic vapour deposition method to form rare-earth activated GaN. J. Phys. D: Appl. Phys. 41, 122001.

Lu X, Beaton D A, Lewis R B, Tiedje T, and Whitwick M B. 2008. Effect of molecular beam epitaxy growth conditions on the Bi content of GaAs1−xBix. APPLIED PHYSICS LETTERS 92, 192110.

Lyon S A. 1986. Journal of Luminescence 35, 121.

Manasevit H M. 1968. Appl. Phys. Lett. 12, 156.

Maximov M V, Ledentsov N N, Ustinov V M, Alferov Z I, Bimberg D, Mater J E. 2000. 29, 476.

Mazzucato S, Zhang T T, Carre` re H, Lagarde D, Boonpeng P, Arnoult A, Lacoste G, Balocchi A, Amand T, Fontaine C, and Marie X. 2013. APPLIED PHYSICS LETTERS 102, 252107.

Mokkapati S and Jagadish C. 2009. III-V compound SC for optoelectronic devices. Materials Today. Volume 12, Volume 12, Issue 4, pp 22-32.

Moussa I, Fitouri H, Rebey A, Jani B E. 2008. Thin Solid Films 516, 8372.

Nave C R. 2016. Evaluating the Lande' g-Factor. http://hyperphysics.phy-astr.gsu.edu/hbase/quantum/Lande.html Access date: 16.01.2017.

Neamen D A. 2003. Semiconductor Physics&Devices, Second Edition.

Neave J H, Joyce B A, Dobson P J, Norton N. 1983. Appl. Phys. A31, 1.

Oe K, Ando S, Sugiyama K. 1977. 1.3μm CW operation of GaInAsP/InP DH diode laser at room temperature. Japanese Journal of Applied Physics, 16, 1273-1274.

Oe K. 2002. Japan. J. Appl. Phys. 41 2801.

Owens A. 2012. Compound Semiconductor Radiation Detectors. Taylor & Francis, pp 49-118.

Palping B R. 1980. Molecular Beam Epitaxy, Pergamon, Oxford.

Parker E H C. 1985. The technology and physics of Molecular Beam Epitaxy, Plenum Press, NY.

Pettinari G, Polimeni A, Capizzi M, Engelkamp H, Christianen P C M, Maan J C, Patane A, and Tiedje T. 2013. Effects of Bi incorporation on the electronic properties of GaAs: Carrier masses, hole mobility, and Bi-induced acceptor states. Physica Status Solidi B 250(4), 779-786.

Polak M P, Scharoch P and Kudrawiec R. 2015. First-principles calculations of bismuth induced changes in the band structure of dilute Ga–V–Bi and In–V–Bi alloys: chemical trends versus experimental data. Semicond. Sci. Technol. 30, 094001.

Rahman M and Hasan N.2016. Compound Semiconductor Epitaxial Growth Techniques. Int. J. Thin. Fil. Sci. Tec. 5, No. 1, 45-49.

Rodrigoa J F, Sales D L, Shafi M, Henini M, Turyanska L, Novikov S, Molinaa S I. 2010. Effect of annealing on the structural and optical properties of 311B GaAsBi layers. Applied Surface Science 256, 5688–5690.

Roy I S. 2012. Characterization of Bismuth Containing Compounds. Department of Microtechnology and Nanoscience. Chalmers University of Technology.

Saint-Cricq N, Landa G, Renucci J B, Hardy I and Cardona M. 1987. Phys. Rev. B 35, 1362.

Sales D L, Guerrero E, Rodrigo J F, Galindo P L, Yáñez A, Shafi A K M, Mari R H, Henini M, Novikov S, Chisholm M F, and Molina S I. 2011. Distribution of bismuth atoms in epitaxial GaAsBi. Applied Physics Letters, 98, 101902-101902-3.

Samajdar D P and Dhar S. 2015. Estimation of Bi induced changes in the direct E0 band gap of III–V-Bi alloys and comparison with experimental data. Physica B 484,27–30.

Samson B, Smith S R P, Dumelow T, Moore K J, and Woodbridge K. 1992. Superlatt. and Microstruct. 11, 403.

Sarcan F, Dönmez O, Kara K, Erol A, Akalın E, Arıkan M Ç, Makhloufi H, Arnoult A and Fontaine C. 2014. Bismuth-induced effects on optical, lattice vibrational, and structural properties of bulk GaAsBi alloys. Nanoscale Research Letters 9:119.

See P and Paul D J. 2001. IEEE Electron Device Lett. 22, 582.

Seong M J, Francoeur S, Yoon S, Mascarenhas A, Tixier S, Adamcyk M, Tiedje T. 2005. Bi-induced vibrational modes in GaAsBi. Superlattices and Microstructures, 37, 394.

Singh J. 2003. Electronic and Optoelectronic Properties of Semiconductor, Cambridge University Press.

Singh J. 2001. Semiconductor Devices, Basic Principles, John Wiley & Sons, Inc.

Shen H, Pollak F H and Sacks R N.1985. Appl.Phys. Lett. 47, 891.

Steele J A, Lewis R A, Henini M, Lemine O M, Fan D, Mazur Yu Dorogan, V. G., Grant P. C., Yu S.Q., and Salamo G. J. 2014. Raman scattering reveals strong LO-phonon-hole-plasmon coupling in nominally undoped GaAsBi: optical determination of carrier concentration. Optics Express, 22, 10, 11680-11689.

Steele J A, Lewis R A, Henini M, Lemine O M, and Alkaoud A. 2013. Raman scattering studies of strain effects in (100) and (311)B GaAs1-x Bix epitaxial layers. J. of Appl. Phys. 19, 114.

Steele J A, Lewis R A, Horvat J, Nancarrow M J B, Henini M, Fan D, Mazur Y I, Schmidbauer M, Ware M E, Yu S Q, Salamo G J. 2016. Surface effects of vapour-liquid-solid driven Bi surface droplets formed during molecular-beam-epitaxy of GaAsBi. Scientific Reports, 6:28860.

Stradling R A and Klipstein P C. 1990. Photoluminescence Characterization, in Growth and Characterization of Semiconductors, ed. IOP Publishing Ltd.

Sweeney, S. J. and Jin S. R. 2013. Bismide-nitride alloys: Promising for efficient light emitting devices in the near- and mid-infrared. Journal of Applied Physics, 113, 043110-043110-6

Tixier S, Adamcyk M, Tiedje T, Francoeur S, Mascarenhas A, WeiP, and Schiettekatte F. 2003. Molecular beam epitaxy growth of GaAs1-xBix. Applied Physics Letters, vol. 82, pp. 2245-2247.

Thijs P J A, Tiemijer L F, Binsma J J M, Van Dongen T. 1994. Progress in long-wavelength strained-layer InGaAs(P) quantum-well semiconductor lasers and amplifiers. IEEE Journal of Quantum Electron. 30, 477-499

Tong H, Marie X, and Wu M W. 2014. Electron spin relaxation in $GaAs_{1-x}Bi_x$: Effects of spin-orbit tuning by Bi incorporation. Journal of Applied Physics 112(6).

Usman M, Broderick C A, Lindsay A,1 and O'Reilly E P. 2011. Tight-binding analysis of the electronic structure of dilute bismide alloys of GaP and GaAs. Condensed matter, Phys. Rev. B 84, 245202.

Varshni Y P. 1967. Physica 34, 149.

Vegard L. 1921. Die Konstitution der Mischkristalle und die Raumfullung der Atome. Z. Physik, 5:17.

Verma P, Oe K, Yamada M. 2001. Raman studies on GaAsBi and InAsBi. J. of Appl. Phys. 89, 1657.

Wolfram Mathematica. 2016. Gallium, Arsenic and Bizmuth. http://periodictable.com/Elements/033/data.html Access date: 29.12.2016

Yeckel A and Derby J J. 2004. Computer Modelling of Bulk Crystal Growth. Bulk Crystal Growth of Electronic, Optical, and Optoelectronic Materials. John Willey&Sons.

Yu P Y and Cardona M. 2010. Fundamentals of Semiconductors, Fourth Edition.